



#### **OPEN ACCESS**

EDITED BY Stefano Cairo, Champions Oncology, Inc., United States

REVIEWED BY

Janith Ananda Seneviratne, Peter MacCallum Cancer Centre, Australia Nevim Aygun, Ege University, Türkiye

\*CORRESPONDENCE

Soraya Epp

soraya.epp@ucd.ie
 soraya.epp@ucd.ie

Walter Kolch

<sup>†</sup>These authors share senior authorship

RECEIVED 17 April 2025
ACCEPTED 29 September 2025
PUBLISHED 24 October 2025

#### CITATION

Epp S, Egan D, Poon E, Abdul Aziz AA, Wynne K, Chesler L, Halasz M and Kolch W (2025) Oxphos targeting of *MYCN*-amplified neuroblastoma. *Front. Oncol.* 15:1613751. doi: 10.3389/fonc.2025.1613751

#### COPYRIGHT

© 2025 Epp, Egan, Poon, Abdul Aziz, Wynne, Chesler, Halasz and Kolch. This is an openaccess article distributed under the terms of the Creative Commons Attribution License (CC BY). The use, distribution or reproduction in other forums is permitted, provided the original author(s) and the copyright owner(s) are credited and that the original publication in this journal is cited, in accordance with accepted academic practice. No use, distribution or reproduction is permitted which does not comply with these terms.

# Oxphos targeting of MYCN-amplified neuroblastoma

Soraya Epp <sup>1\*</sup>, Donagh Egan <sup>1</sup>, Evon Poon <sup>2</sup>, Amirah Adlina Abdul Aziz <sup>1</sup>, Kieran Wynne <sup>1</sup>, Louis Chesler <sup>2</sup>, Melinda Halasz <sup>1,3†</sup> and Walter Kolch <sup>1,3\*†</sup>

<sup>1</sup>Systems Biology Ireland, University College Dublin, School of Medicine, Dublin, Ireland, <sup>2</sup>Division of Clinical Studies, The Institute of Cancer Research, London, United Kingdom, <sup>3</sup>Conway Institute of Biomolecular and Biomedical Research, University College Dublin, Dublin, Ireland

High risk - neuroblastoma (HR-NB) is a pediatric solid tumor with high lethality. Half of HR-NB are driven by MYCN gene amplification (MNA). These HR-NBs require high dosage chemotherapy and often relapse. Moreover, current therapies can cause severe long-term side effects and new therapies are urgently needed. This study investigates a novel therapeutic approach targeting the metabolic vulnerabilities of MNA NB cells. We discovered that Diphenyleneiodonium chloride (DPI), an inhibitor of flavoprotein enzymes and mitochondrial complex I, synergizes with mitoguinone mesylate (MitoQ), a mitochondria-targeted antioxidant in 2D and 3D in vitro models of NB. Similarly to DPI, MitoQ appears to have a greater effect on cells with higher MYCN levels. Furthermore, low nanomolar concentrations of MitoQ significantly decrease MYCN protein expression and induce differentiation of MNA cells. The DPI and MitoQ combination further synergizes with vincristine, a chemotherapeutic agent used in NB treatment. Phosphoproteomics and proteomics analysis suggests that the drug combination induces MNA NB cell death by arresting the cell cycle and inhibiting oxidative phosphorylation (OXPHOS) in the mitochondria. Thus, interference with mitochondrial metabolism may represent an effective strategy to enhance the activity of chemotherapeutic drugs in MNA-NB.

KEYWORDS

 $\hbox{childhood cancer, neuroblastoma, combination therapy, oxidative stress, DPI, } \\ \hbox{MitoQ, metabolism}$ 

#### 1 Introduction

Neuroblastoma (NB) is the most common extracranial solid tumor in infants. NBs originate from neural crest cells and typically form in the abdominal or thoracic regions in paraspinal ganglia (1). Despite comprising only 6% of all pediatric cancers, NB accounts for 15% of all childhood cancer-related deaths (2). NB is unique due to its clinical bipolarity: favorable with occasional spontaneous regression, or unfavorable, with highly aggressive behavior and metastatic spread (1, 3). Despite considerable progress in improving survival rates, the overall 5-year event-free survival for high-risk patients (ca. 40% of all NB

patients) is still less than 50%. High-risk patients are often treated with a combination of intensive genotoxic chemotherapy and radiation therapy. However, a large proportion of patients relapses, leaving them with limited or no treatment options. Furthermore, genotoxic therapies can result in significant long-term side effects, such as hearing loss, secondary cancers, infertility, and endocrine deficiencies (4).

MYCN is a transcription factor belonging to the highly homologous *MYC*-family of cellular oncogenes, ubiquitously expressed in mammals. *MYCN* amplification (MNA) occurs in ca. 20% of NB patients and drives half of the aggressive forms of the disease with poor outcomes (1). Pharmacologic inhibition of MYCN is very challenging due to the absence of drug-binding pockets in the MYCN protein, and no FDA-approved treatment is currently available (5). Thus, efforts have focused on strategies to block MYCN indirectly, e.g. via inhibition of the *MYCN* transcriptional machinery, synthetic lethality, and destabilization of the MYCN protein (6, 7).

NB, like other malignancies, is associated with modifications in cellular metabolism that may contribute to oncogenesis. Activation of oncogenes and loss of tumor suppressors lead to the increased production of superoxide via mitochondria and NADPH oxidase (NOX) pathways (8, 9). Superoxide is subsequently converted to hydrogen peroxide (H<sub>2</sub>O<sub>2</sub>), a more stable and stronger oxidizing molecule, through the action of superoxide dismutase enzymes (SOD). H<sub>2</sub>O<sub>2</sub> can oxidize proteins and lipids, but also act as a signaling molecule modulating various cellular processes linked to oncogenesis (10). As a result, malignant cells need to control the concentration of H2O2 precisely to avoid excessive oxidative damage, while enabling the pro-tumorigenic effects of H2O2 signaling. MNA cells rely on an elevated antioxidant response through the Xc-/glutathione (GSH) pathway to scavenge lipid hydroperoxides, a by-product formed from excess H<sub>2</sub>O<sub>2</sub> (11, 12). The preference for using oxidative phosphorylation (OXPHOS) to meet energy demands, and the resulting increase in reactive oxygen species (ROS) has been shown to be a targetable vulnerability of MNA cells (8, 12, 13). Recently, several studies have demonstrated the ability of MYCN to regulate mitochondrial genes in NB, and more specifically complex I genes of the electron transport chain (ETC) (14, 15).

We recently discovered in a drug screen that Diphenyleneiodonium chloride (DPI) selectively induces cell death of MNA NB cells *in vitro* and decreases tumor growth *in vivo* (16). DPI is an inhibitor of flavoprotein enzymes, including NOX, and the mitochondrial complex I. It has a wide spectrum of metabolic effects, including induction of apoptosis via ROS production and cytochrome c release (17), inhibition of NADH oxidation (18), and loss of GSH (19). DPI has also been employed in numerous studies as a ROS inhibitor due to its demonstrated efficacy in reducing superoxide production during reverse electron transport (20, 21). However, identifying the specific ROS generation site and the precise mode of DPI action has proven challenging and appears to be contingent upon contextual factors (22, 23). We also demonstrated that DPI significantly increases mitochondrial ROS production in MNA cells, but not in non-MNA cells, indicating a

MYCN-dependent effect (16). To investigate the role of ROS and the mechanism of action of DPI in MNA cells, we employed a widely and commercially available mitochondria-targeted antioxidant, mitoquinone mesylate (MitoQ). Unexpectedly, we observed that DPI and MitoQ synergize, prompting us to examine how their combination affects cell viability, both alone and together with vincristine, a chemotherapeutic used in high-risk NB.

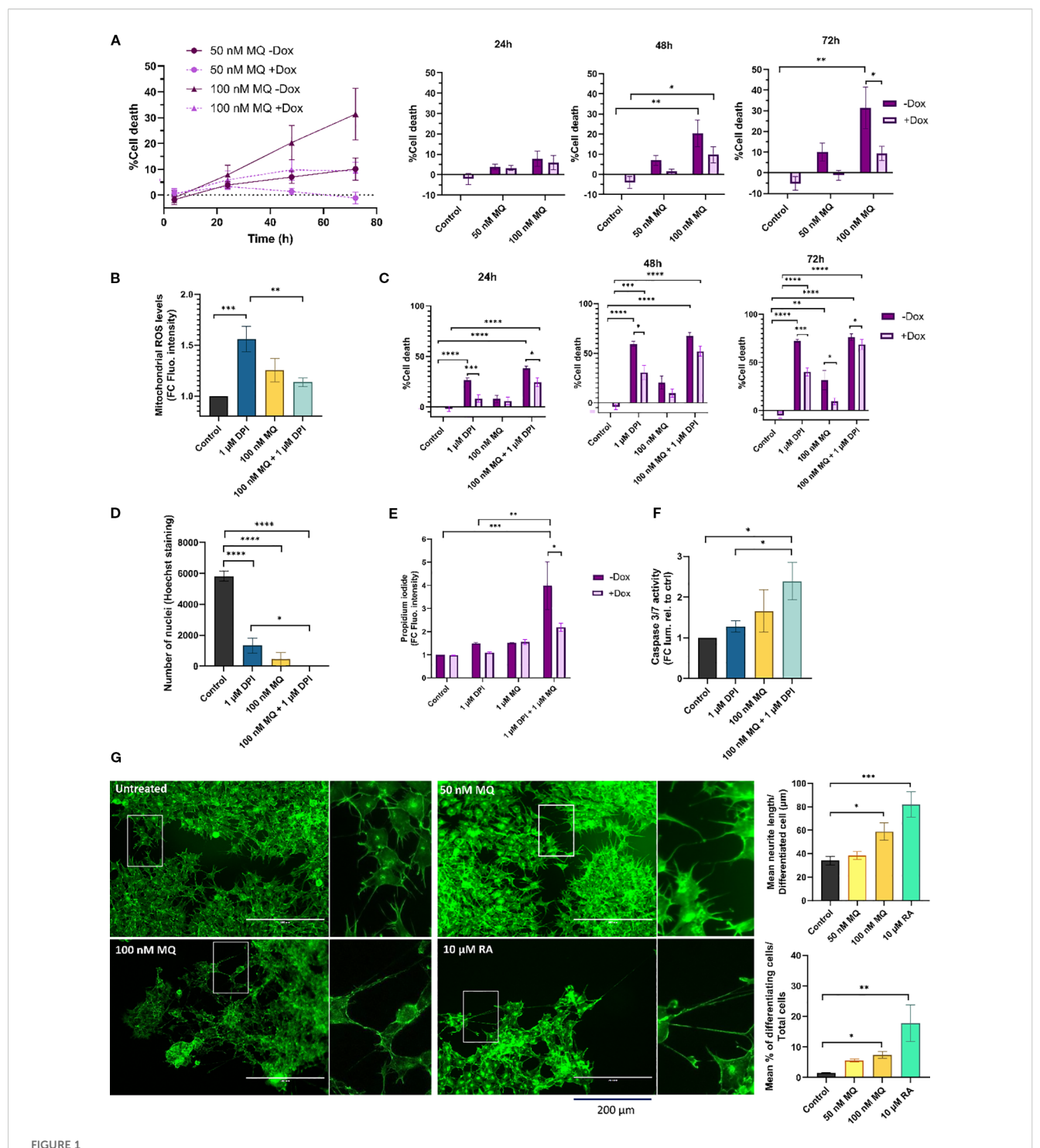
Although precision therapy for individual patients remains limited, combination therapy has the potential to enhance treatment efficacy while potentially reducing reliance on highly toxic chemotherapy (24). Multiple drug combinations have several advantages over monotherapy, as they can achieve higher efficacy and, by using lower drug doses, reduce the risk of adverse effects and acquired resistance (25). As a result, combination therapies are widely utilized in the treatment of cancer (26), although primarily involving genotoxic drugs for the treatment of NB. To address this issue, we evaluated a potential triple combination therapy, comprising two metabolic-targeting drug and a chemotherapeutic agent, aiming to develop a more effective therapeutic approach for MNA NB.

#### 2 Results

## 2.1 MitoQ induces cell death and differentiation in neuroblastoma cells and potentiates DPI-induced cytotoxicity

To investigate whether enhanced ROS production mediates the cytotoxic effects of DPI, we used MitoQ, a ROS scavenger that selectively accumulates in mitochondria (27, 28). First, we assessed the viability of the MNA IMR-5/75 cells in response to MitoQ. In these cells MYCN protein expression can be downregulated by ca. 50% by a doxycycline inducible shRNA (29) (Supplementary Figure S1). We found that MitoQ was non-cytotoxic up to a concentration of 100 nM over a 24-hour treatment period (Figure 1A). Then, we tested the antioxidant effect of MitoQ when combined with DPI. Mitochondrial superoxide production was measured using the selective fluorogenic MitoSOX Red dye (30). DPI is known to increase mitochondrial superoxide production in a dose dependent manner in MNA cells (16). Unexpectedly, MitoQ on its own increased ROS concentrations, although the effect was not significant (Figure 1B). Combining DPI and MitoQ effectively suppressed DPI-induced superoxide production to almost baseline level (Figure 1B).

To determine whether cell death follows the pattern of superoxide levels recorded in DPI and MitoQ-treated IMR-5/75 cells, cell toxicity was measured using the CellTox Green Dye that detects modifications in membrane integrity resulting from cell death (Figures 1A, C). As previously shown, DPI induced progressive cell death over the three-day observation period, which was significantly mitigated by downregulation of MYCN (16) (Figure 1C). 100 nM MitoQ on its own was significantly cytotoxic at day 2 and 3, an effect which was also lessened by



MitoQ induces cell death and differentiation and enhances DPI-induced cytotoxicity in MNA NB cells. (A) CellTox Green dye was used to determine cytotoxicity of IMR-5/75 cells -/+ Dox treated with MitoQ over a period of 72 hours. Bar charts (right) show detailed values and statistical significance at individual time points vs. control. +Dox: shRNA targeting MYCN induced and MYCN expression reduced; -Dox: shRNA targeting MYCN not induced. (B) MitoSOX Red dye was used to measure mitochondrial superoxide production in IMR-5/75 treated with DPI and MitoQ alone or in combination for 2 hours. (C) CellTox Green dye was used to determine cytotoxicity of IMR-5/75 cells -/+ Dox treated with DPI and MitoQ alone or in combination over a period of 72 hours. (D) Nuclei of IMR-5/75 cells were visualized by Hoechst staining after 72 hours of treatment with either DPI or MitoQ on their own or in combination. (E) Propidium lodide staining was observed by confocal microscopy to quantify cell death in IMR-5/75 following a 24-hour treatment with 1 μM DPI, 1 μM DPI MitoQ or a combination of both in -Dox and +Dox cells. (F) Caspase-Glo 3/7 was used to determine caspases 3/7 activation in IMR-5/75 cells treated with DPI and MitoQ alone or in combination for 24 hours. (G) Neuronal differentiation was assessed by phalloidin staining of IMR-5/75 cells treated with 50 nM or 100 nM MitoQ for 7 days. 10 μM retinoic acid was used as a positive control to induce neurite outgrowth. Were taken into consideration cells with neurites >= 2 cell body diameters. Scale bar = 200 μm. (Mean ± SEM; n=3; Ordinary One-Way ANOVA or Two-Way ANOVA for -Dox/+Dox comparisons, p<0.05 = \*\*, p<0.005 = \*\*\*, p<0.0005 = \*\*\*\*, p<0.00

0<0.0001 = ^^^^)

downregulation of MYCN (Figures 1A, C). However, MitoQ failed to reduce DPI-induced cell death at all tested time points (Figure 1C). Cell death was further assessed by counting nuclei and Propidium Iodide (PI) staining (Figures 1D, E). Nuclei counting of IMR-5/75 cells treated with the same conditions (Figure 1D) for 72h confirmed the cell toxicity results (Figure 1C). Combining MitoQ and DPI resulted in complete disappearance of nuclei, indicating extensive cell death. PI cannot penetrate intact cell membranes and thus only stains cells whose membrane integrity is compromised, such as apoptotic or necrotic cells. While 100 nM MitoQ only minimally increased DPI-induced cell death (Figure 1C), higher MitoQ concentrations significantly enhanced DPI-mediated cell toxicity as measured by an increased PI uptake after 24h, in a MYCN-dependent fashion (Figure 1E). Consistent with these findings, caspase-3/7 activity showed a modest, non-significant increase with MitoQ alone after 24h, but was elevated when MitoQ was combined with DPI. 1 µM DPI alone did not increase caspase activity, although higher doses are required to trigger caspase activation, as shown previously (16).

These results suggest that the cytotoxicity observed following treatment with MitoQ alone and in combination with DPI is not solely dependent on its ability to regulate mitochondrial superoxide production in MNA NB cells, which is in line with recent studies on MitoQ effects in other cancer cell types (31, 32). Interestingly, the cytotoxic effects of MitoQ were amplified by higher MYCN levels. Moreover, caspase-3/7 activation is consistent with engagement of the intrinsic, mitochondrial apoptotic pathway.

The arrested differentiation of neuroblasts is a characteristic of NB tumorigenesis and invasiveness (33). To assess whether MitoQ treatment can similarly overcome the differentiation block observed with DPI (16), MNA IMR-5/75 cells were treated every two days with either 50 nM or 100 nM MitoQ and monitored by microscopy (Figure 1G). Neurite outgrowth was visualized and quantified using Phalloidin staining, which specifically binds to actin filaments. 100 nM MitoQ treatment resulted in differentiation as evidenced by an increase in neurite outgrowth 7 days after treatment, compared to the non-treated control. 10  $\mu$ M retinoic acid was used as a positive control for maturation towards a differentiated neuronal phenotype, as shown previously (34). These results suggest that MitoQ slows down cell growth, induces cell death and differentiation of MNA NB cells.

### 2.2 DPI synergizes with MitoQ in MNA NB cells

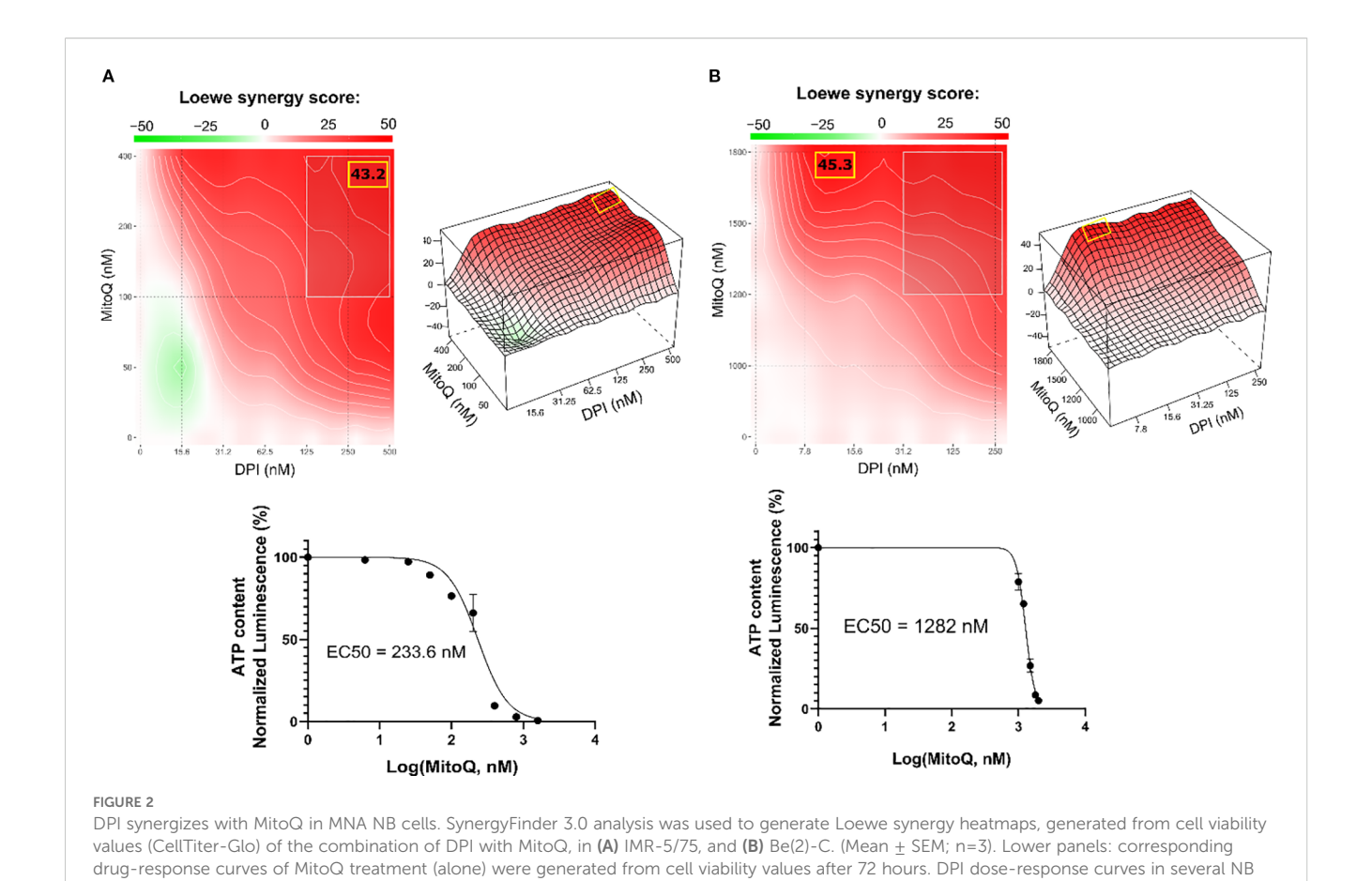
To assess whether MitoQ and DPI act synergistically in reducing cell viability, we treated two MNA NB cell lines (IMR-5/75 and Be(2)-C) with various concentrations of DPI and MitoQ. Synergy was assessed using SynergyFinder 3.0 (35), which computes synergy scores based on different mathematical models. Given that both MitoQ and DPI target mitochondrial function, we used the Loewe synergy model, which is particularly suited for evaluating the combined effects of drugs with similar mechanisms of action (36). The combination exhibited a pronounced synergistic effect in both MNA

NB cell lines (Figures 2A, B). Although the concept of combination synergy is highly dependent on the underlying assumptions (37), according to SynergyFinder 3.0 the synergy scores can be interpreted as follows: from -10 to 10 the interaction is likely to be additive, larger than 10 the interaction is likely to be synergistic, and conversely, if the score in less than -10, then the interaction between the two drugs is most likely antagonistic. In IMR-5/75, the highest Loewe score is 43.2 and obtained at ~400 nM MitoQ combined with ~500 nM DPI (Figure 2A). The highest Loewe score in Be(2)-C is 45.3 and reached at ~1800 nM MitoQ combined with ~10 nM DPI (Figure 2B). The highest score was reached with a ~4.5fold lower concentration of MitoQ in IMR-5/75 than in Be(2)-C cells, which seem to be more resistant to treatment (Figures 2A, B). These results are in line with previous findings indicating that inhibition of mitochondrial complex I synergizes with mitochondrial antioxidants in impairing cancer cell fitness, supporting the notion that complex I is a dominant determinant of viability (28).

## 2.3 DPI synergizes with vincristine and MitoQ in reducing cell viability of MNA NB cells

Finding synergistic drug combinations allows for combining drugs at lower concentrations, which is an important strategy for enhancing therapeutic efficacy while minimizing adverse effects. Vincristine (vin) is a commonly used chemotherapeutic agent for treating patients with NB. As genotoxic treatment is clinically very effective but also toxic, we tested whether DPI could reduce the dosage of vincristine required for efficient cancer cell killing. A DPI and vincristine combination was tested for synergy in the two MNA NB cell lines IMR-5/75 and Be(2)-C (Figures 3A, B). To evaluate this combination, we used the Zero Interaction Potency (ZIP) model, which accounts for independent drug effects and is particularly suited for combinations of agents with differing targets, such as DPI and vincristine (38). ZIP scores of >10 are considered to indicate synergy (35). The combination showed synergistic effects in reducing cell viability in IMR-5/75 and Be (2)-C cells. In IMR-5/75, the highest ZIP score is 11.3 and reached at ~0.75 nM vincristine combined with ~100 nM DPI (Figure 3A). The highest ZIP score in Be(2)-C is 13.7 and observed for ~15 nM vincristine combined with ~30 nM DPI (Figure 3B). These results indicate that vincristine and DPI have an additive/synergistic interaction in MNA cells for reducing cell viability at low concentrations that are clinically achievable.

Given the synergy of DPI with both MitoQ and vincristine, we combined all three drugs at reduced dosage. To assess synergy of the 3-drug combination, the Bliss Independence model was used (39) (Figures 3C–E). The model is based on the premise that the relative effect of a drug is independent of the presence of the other drug. When two or more independent drugs are combined, their effects add up, and the Bliss synergy score is 0 (39). Within the Bliss independence model calculation, synergy is assumed when the actual effect of the combination is greater than the expected effect, i.e., if the Bliss score is greater than 0 (40). For a 2-drug combination (MitoQ + DPI, (M+D)/2),



the drugs were tested at their IC50 concentration divided by 2 or for a 3-drug combination (MitoQ + DPI + vin, (M+D+V)/3) divided by 3. For both MNA NB cell lines tested, the IC50/2 and IC50/3 combinations displayed similar or slightly greater effects in reducing cell viability than the IC50 concentration of each of the single drugs. Indeed, for all the combinations, the Bliss score was > 0 in the two MNA NB cell lines (Figures 3D, E). Therefore, the double and triple combinations at reduced doses are synergistic in reducing the cell viability of IMR-5/75 and Be(2)-C.

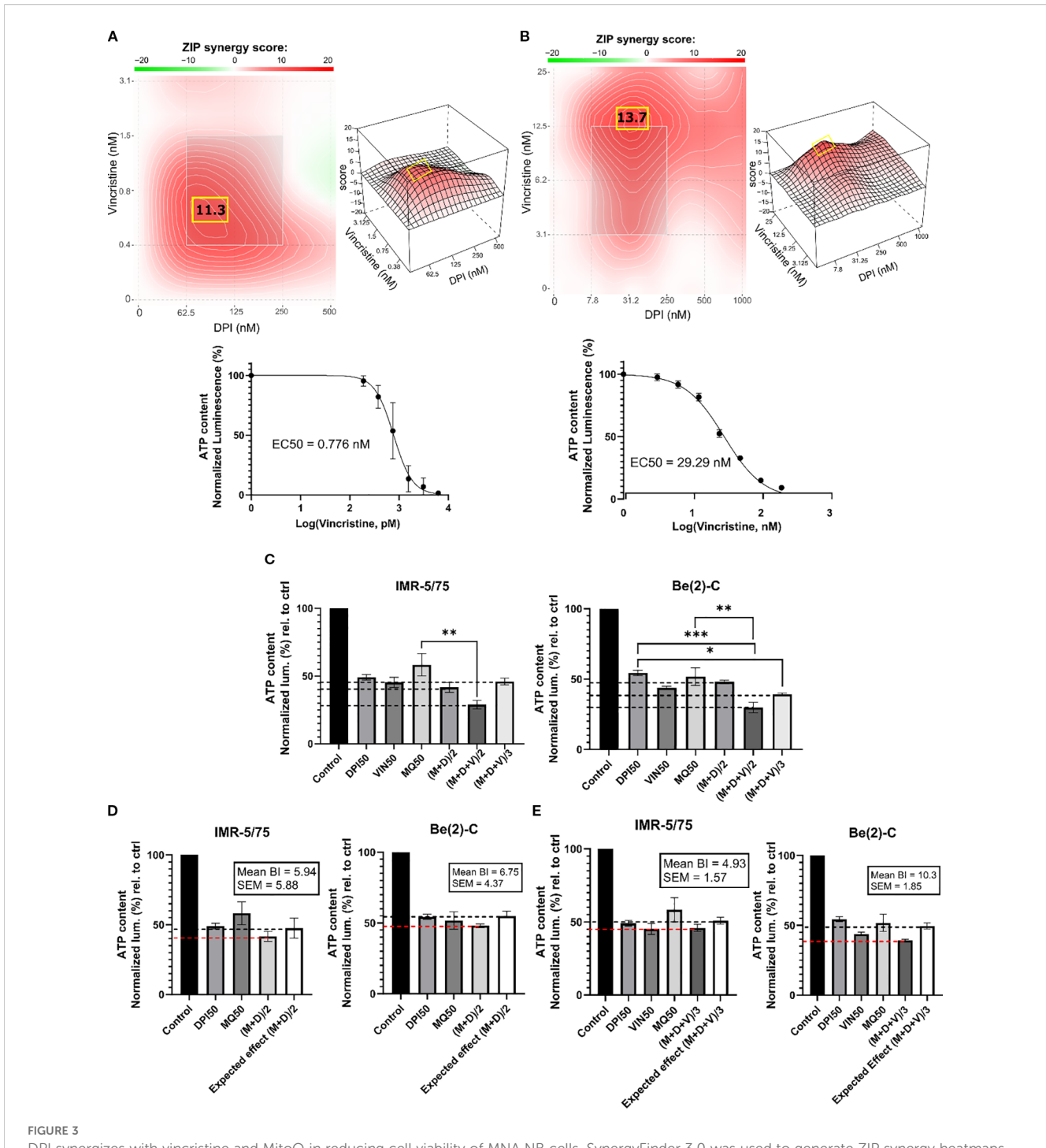
cell lines have been previously published (16). (Mean + SEM; n>3).

### 2.4 Combining DPI, MitoQ and vincristine induces cell death of MNA NB cells

To characterize the interaction between MitoQ, DPI, and vincristine, we assessed their effects on cell death at IC50/2 and IC50/3 concentrations in four NB cell lines: Be(2)-C (MNA), IMR-32 (MNA), IMR-5/75 (MNA with MYCN downregulatable), and SH-SY5Y/MYCN (non-MNA, MYCN-inducible). The Be(2)-C cell line showed greater resistance with IC50s higher than other tested cell lines. Therefore, in order to assure that the drug sensitivity range is covered in full, the IC50 concentrations of Be(2)-C cells for the 3 drugs were taken as a basis to treat all other cell lines. Cell toxicity was measured using CellTox Green (Figure 4). The double combination ((M+D)/2) significantly increased toxicity in IMR-32

and IMR-5/75 cells within 24 hours, persisting up to 72 hours. However, in Be(2)-C cells, it reduced ATP content by more than half (Figure 3D) without increasing cell death (Figure 4A), indicating a cytostatic rather than cytotoxic effect. In Be(2)-C, significant toxicity occurred only after 72 hours with the triple combination ((M+D+V)/3) (Figure 4C). In SH-SY5Y/MYCN cells, (M+D)/2 had no effect on cell death, while (M+D+V)/3 increased toxicity at 48 and 72 hours (Figure 4A). MYCN abundance modestly influenced sensitivity: MYCN downregulation in IMR-5/75 cells slightly reduced toxicity, while MYCN induction in SH-SY5Y/MYCN slightly increased it, though neither change reached significance. Although MYCN downregulation or overexpression are in the region of 50% or more, they are still within the natural range of variation observed in MNA and MYCN non-amplified cells, respectively (41, 42). This suggests that modest changes in MYCN alone are not sufficient to strongly alter sensitivity under our experimental conditions. Overall, the triple-drug combination was effective in inducing cell death across four high-risk NB cell lines. The double-drug combination promoted cell death in two MNA cell lines, but in the more resistant MNA Be(2)-C cells it primarily caused metabolic inactivity.

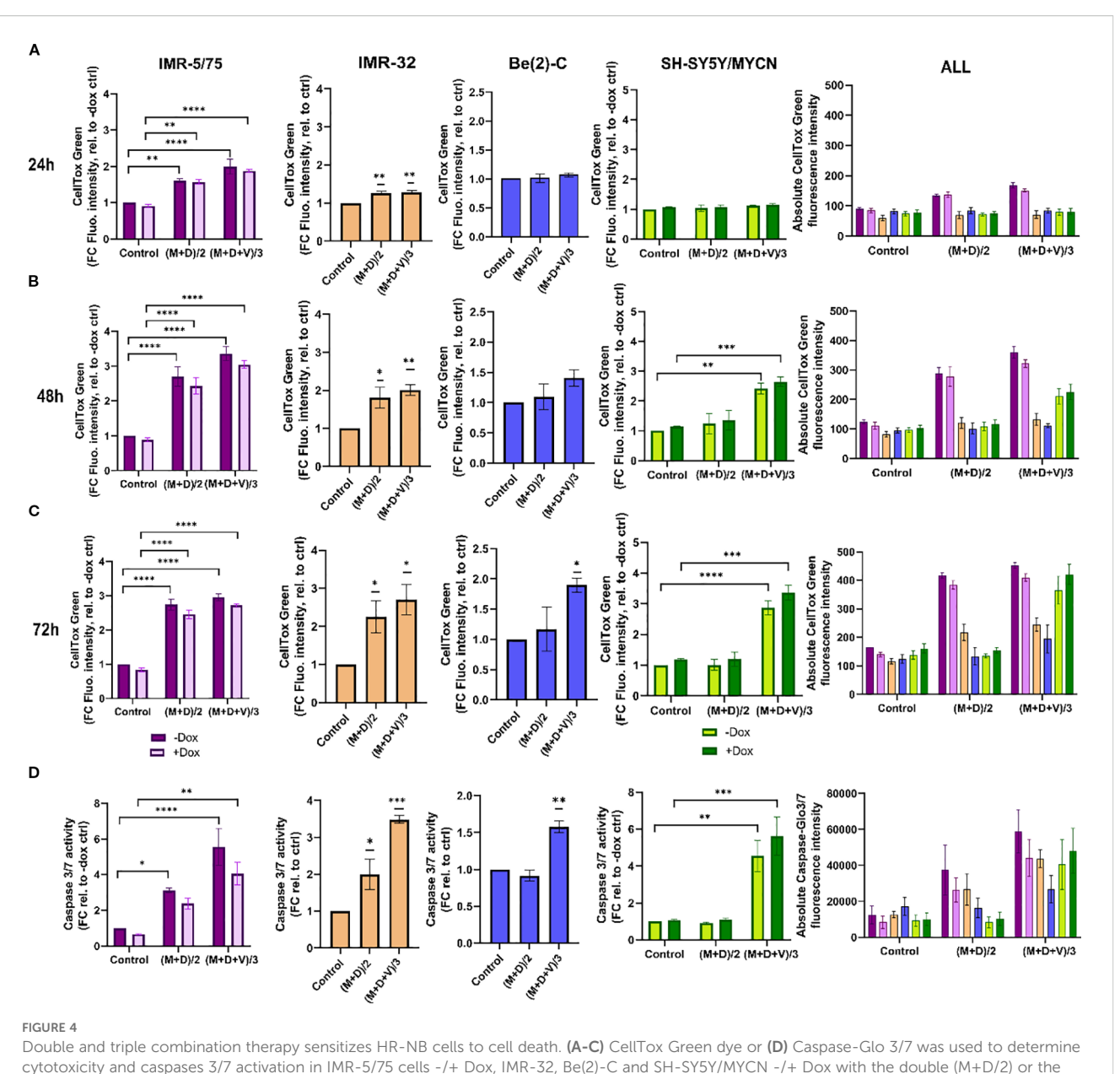
To further measure cell death upon treatment with MitoQ, DPI and vincristine, we measured caspase 3/7 activation using Caspase-Glo 3/7 (Promega) (Figure 4D). Caspases 3 and 7, key mediators of the mitochondrial apoptotic pathway, were significantly activated



PFIGURE 3
DPI synergizes with vincristine and MitoQ in reducing cell viability of MNA NB cells. SynergyFinder 3.0 was used to generate ZIP synergy heatmaps from cell viability values (CellTiter-Glo) of the combination of DPI with vincristine, in (A) IMR-5/75, and (B) Be(2)-C after 72 hours of treatment. Lower panels: corresponding drug-response curves of vincristine treatment (alone) were generated from cell viability values after 72 hours. (C) IMR-5/75 and Be(2)-C cells were treated with reduced IC50 doses of MitoQ, DPI and vincristine. (M = MitoQ, D = DPI, and V = vincristine). (D, E) The Bliss Independence model was used to assess synergy, additivity or antagonism of the double and triple drug combination at a reduced dose in IMR-5/75 and Be(2)-C MNA cells. Dashed black lines indicate the expected effect, and the dashed red lines the observed effect. (Mean ± SEM; n=3; Ordinary One-Way ANOVA, p<0.05 = \*\*, p<0.005 = \*\*\*, p<0.0005 = \*\*\*\*).

by (M+D)/2 after 24 hours in IMR-5/75 -Dox and IMR-32, but not in Be(2)-C and SH-SY5Y/MYCN cells. (M+D+V)/3 enhanced caspases 3/7 activation in all cell lines tested. Downregulating MYCN in IMR-5/75 decreased caspase activation for both treatments, while inducing MYCN expression in SH-SY5Y/

MYCN increased caspase activation, although the differences were not statistically significant (Figure 4D). These data suggest that MNA NB cells exhibit great sensitivity to the triple drug combinations. The non-MNA cell line SH-SY5Y/MYCN showed no sensitivity to the double combination, similarly to the most



Double and triple combination therapy sensitizes HR-NB cells to cell death. (A-C) CellTox Green dye or (D) Caspase-Glo 3/7 was used to determine cytotoxicity and caspases 3/7 activation in IMR-5/75 cells -/+ Dox, IMR-32, Be(2)-C and SH-SY5Y/MYCN -/+ Dox with the double (M+D/2) or the triple (M+D+V/3) combination after (A) 24h, (B) 48h and (C) 72h of treatment. Caspases activation was measured at 24h. (Mean  $\pm$  SEM; n=3; Ordinary One-Way ANOVA or Two-Way ANOVA for -/+ Dox cell lines, p<0.05 = \*\*, p<0.005 = \*\*\*, p<0.0005 = \*\*\*\*, p<0.0001 = \*\*\*\*\*). In the non-MYCN-amplified SH-SY5Y/MYCN cells, the expression of MYCN is doxycycline-inducible (+Dox: expression of the MYCN transgene induced; -Dox: MYCN transgene not induced).

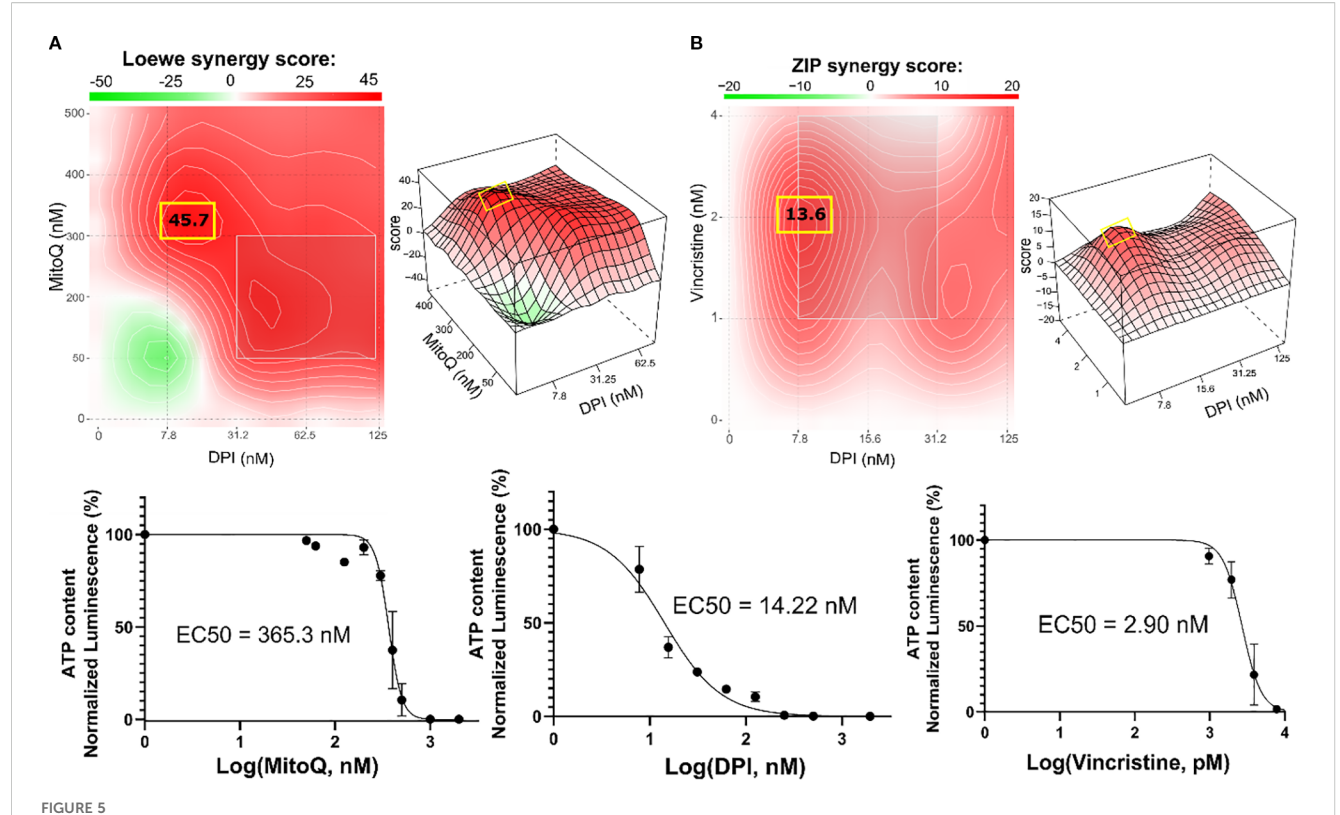
resistant MNA cell line, Be(2)-C. Combining compounds having a synergistic interaction enables the use of reduced concentrations while still inducing cell death and caspase activation at a high level.

## 2.5 Combination therapy inhibits the growth of Th-MYCN mouse NB spheroids

To assess the antitumor potential of the dual and triple drug combinations in a more physiological model than cell lines, we used a 3D spheroid model of a transgenic mouse that overexpresses MYCN under the control of the tyrosine hydroxylase (Th)

promoter. This promoter is active in neural crest cells, and driving *MYCN* overexpression in these progenitor cells of NB causes the animals (Th-*MYCN*) to develop tumors that closely resemble human NB (43). Spheroid tumor models are 3D aggregates of cancer cells which mimic the architecture and cellular heterogeneity of tumor tissue *in vitro*. They are viewed as an intermediate model between 2D monolayers and animal models, as they preserve key features of tumors, especially the response to drug treatments (44).

Treating the Th-MYCN spheroids with the DPI-MitoQ combination showed a strong synergistic effect. The highest Loewe score was 45.7, achieved when  $\approx 300$  nM MitoQ is



Combination therapy inhibits the growth of Th-MYCN mouse NB spheroids. SynergyFinder 3.0 analysis was used to generate Loewe and ZIP synergy heatmaps, generated from cell viability values (CellTiter-Glo) of the combination of (A) DPI with MitoQ, and (B) DPI with vincristine in Th-MYCN spheres. Lower panels: corresponding drug-response curves of DPI, MitoQ and vincristine single treatments were generated from cell viability values after 72 hours. (Mean ± SEM; n>3).

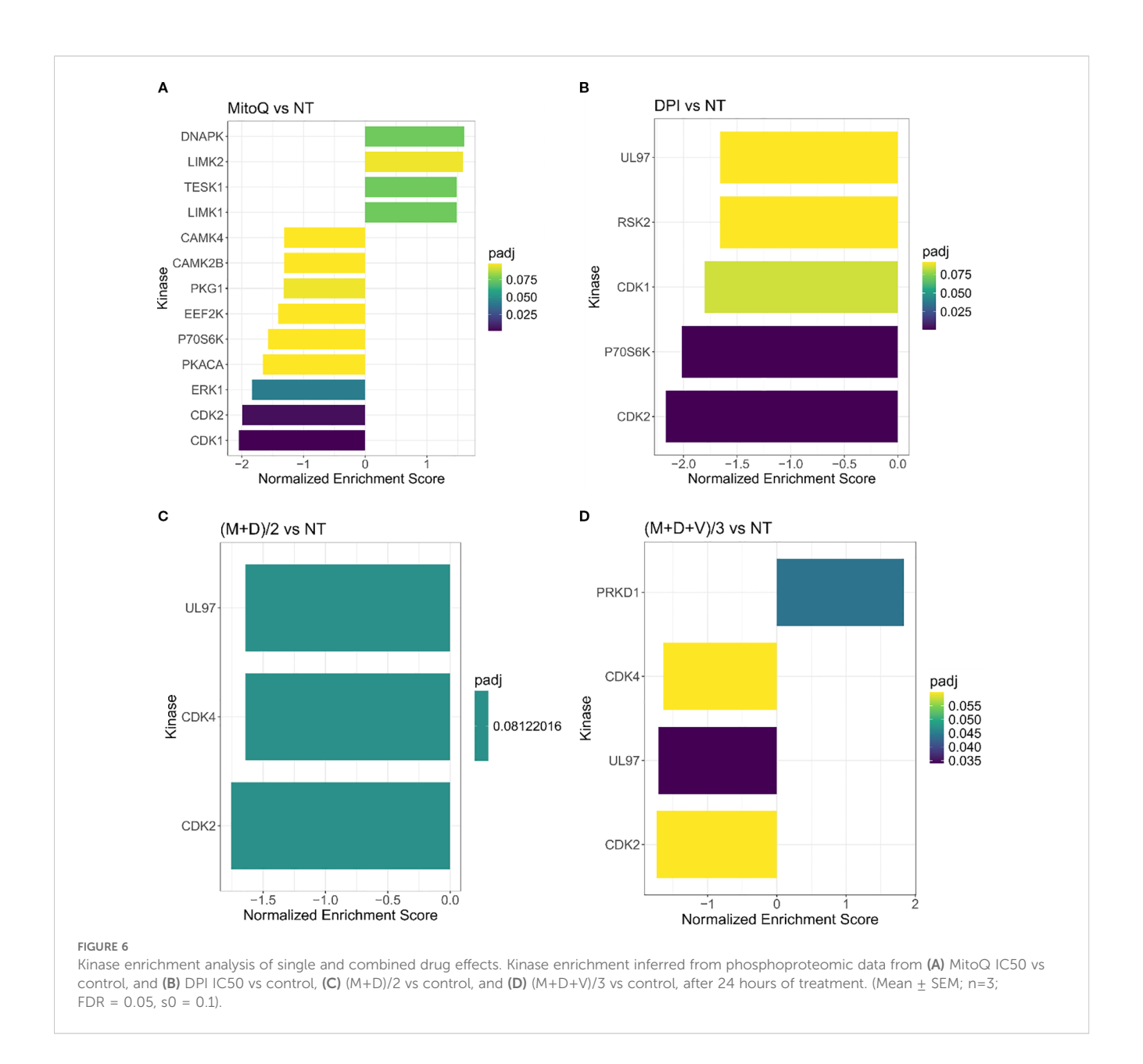
combined with  $\approx$  7.8 nM DPI (Figure 5A). The combination between DPI and vincristine was also synergistic but less potent. Peak synergy occurred when  $\approx$  2 nM vincristine was combined with 7.8 nM DPI, with an associated ZIP score of 13.6 (Figure 5B). Interestingly, the synergy maps for both MitoQ-DPI and vincristine-DPI are highly similar to those observed in Be(2)-C cells. Moreover, the IC50 values of MitoQ, DPI and vincristine are within the range observed for IMR-5/75 and Be(2)-C MNA cell lines (Figures 2A, B; Figures 3A, B). These correlations show that 2D and 3D culture models of MNA behave very similarly in terms of drug responses, which validates drug screening in 2D cultures as not only as convenient but also meaningful method for finding new therapies for MNA.

In addition to assessing cell viability, DNA damage was visualized by PI (45, 46) and Hoechst staining of Th-MYCN spheres following exposure to M+D and M+D+V combinations (Supplementary Figure S2). The drugs were used at their IC50 concentrations to maximize synergy and induce a high rate of cell death. After 24 hours, both the double and the triple combinations increased cell death. The visual increase in Hoechst fluorescence intensity following M+D and M+D+V treatments can be explained by accumulation of the dye due to highly condensed and fragmented DNA (46). This observation confirms that the corresponding increase in PI intensity is due to apoptotic processes (Supplementary Figure S2).

## 2.6 Investigating the mechanism of drug interaction by proteomic and phosphoproteomic analysis

To elucidate the synergistic mechanism of our double and triple drug combinations, we examined the proteomics and phosphoproteomics changes in MNA Be(2)-C cells treated with DPI+/-MitoQ+/-Vin for 24 hours by mass spectrometry (MS). The Be(2)-C cell line was selected due to its similar response profile as spheroids and delayed response to treatment compared to both MNA NB cell lines IMR-5/75 and IMR-32. Indeed, Be(2)-C cells only significantly apoptose after 72 hours of (M+D+V)/3 treatment (Figure 4C), allowing a broad time window to identify pathways that mediate apoptosis-associated signaling.

First, we assessed protein expression in Be(2)-C cells treated with either MitoQ IC50, DPI IC50, vin IC50 or the double and triple drug combinations, versus control (Supplementary Figures S3-S6; Supplementary Table S1). Protein enrichment analysis showed that DPI and MitoQ single treatments induced a similar profile of downregulated peptides, affecting mainly members of the complex I of the mitochondrial respiratory chain and cell cycle/division proteins (Supplementary Figures S3, S4; Supplementary Table S1). However, they exerted contrasting effects on proteins involved in histone H3-K27 and H3-K4 trimethylation, with DPI causing downregulation and MitoQ causing upregulation. MitoQ



upregulated the expression of proteins involved in cellular amino acid synthesis, and hydrogen peroxide catabolic processes. On the other hand, DPI mainly upregulated members of the cholesterol biosynthetic process (Supplementary Figure S4; Supplementary Table S1). At its IC50 concentration, vincristine induced significant downregulation of Ribonucleotide Reductase M2 (RRM2), involved in DNA damage repair and cell cycle regulation (Supplementary Table S1). In agreement with their single-drug effects, both (M+D)/2 and (M+D+V)/3 downregulated proteins linked to mitochondrial ATP synthesis and cell cycle (Supplementary Figures S5, S6; Supplementary Table S1). (M+D)/2 upregulated TTC5 and HMGCR, involved in p53-dependent apoptosis and cholesterol metabolic process, respectively (Supplementary Table S1). The triple combination

upregulated UBE2C, TTC5, ELOVL5 and NDUFS8. These proteins are implicated in mitosis, fatty acid metabolism, p53-dependent apoptosis and complex I of the mitochondrial respiratory chain, respectively (Supplementary Table S1). Interestingly, the DNA damage repair protein RRM2, often upregulated in NB to support oncogenicity, was upregulated across all conditions, and phosphorylation at the Ser-80 and Ser-86 sites was significantly downregulated by both combinations (Supplementary Table S1) (47–49).

Based on the phosphoproteomic profiling we then inferred the upstream kinases responsible for the differential phosphorylation observed in each treatment versus control, using a kinase enrichment analysis (Figure 6). Biological functions highly represented by the inferred kinases for both MitoQ and DPI

single treatments include cell cycle regulation, DNA damage response and cell proliferation (DNAPK, CDK1, CDK2, RSK2, P7056K, UL97) (Figures 6A, B). UL97 is a viral protein kinase that shares substrates with CDK1 (50). DNA damage response and regulation of cytoskeleton organization were also prominently represented in MitoQ IC50 treatment compared to control (LIMK1, LIMK2, TESK1, CAMK4, CAMK2B, PKACA, ERK1) (Figure 6B). Moreover, MitoQ decreased MYCN phosphorylation at the Ser-156 residue (Supplementary Table S2). No upstream kinases were predicted for vincristine on its own. For the double and triple combinations, the abundance in phosphorylation marks suggested that mainly kinases linked to cell cycle and cell proliferation are differentially regulated (UL97, PRKD1, CDK2, CDK4) (Figures 6C, D).

Together, proteomic and phosphoproteomic profiling highlighted cell cycle and proliferation pathways as key targets of the double and triple drug combinations (Figures 6C, D; Supplementary Figures S5, S6). MitoQ, DPI and the double drug combination decreased the expression of cyclin D1 (G1/S-phase) and cyclin B1 (G2/M phase), suggesting an inhibitory effect on cell cycle progression. These findings were confirmed by Western blotting (Supplementary Figure S7A). Similarly, the (M+D+V)/3 combination decreased the expression of cyclin B1 and based on Western blot data, also downregulated cyclin D1. Vincristine caused a sharp increase in histone 3 phosphorylation at serine 10 (pS10-H3), likely due to its interference with mitotic spindle assembly, causing mitotic arrest (Supplementary Figure S7A). Since pS10-H3 is a marker for chromosome condensation linked to mitosis, cellular stress (51) and DNA damage (52), its elevation in the triple drug combination likely reflects both a proliferation block and a stress response to vincristine.

According to the MS results, MitoQ and to a lesser extent DPI single treatments reduced MYCN protein levels. These findings were confirmed by Western blotting (Supplementary Figure S7). However, this effect was not observed in Be(2)-C cells treated with the double and triple combinations (Supplementary Figure S7A). In contrast, in the IMR-5/75 MNA cell line, (M+D)/2 reduced MYCN by half, while (M+D+V)/3 led to an even greater decrease (Supplementary Figure S7B). This discrepancy may be related to the finding that Be(2)-C cells are more resistant to treatment and undergo apoptosis at a later time point.

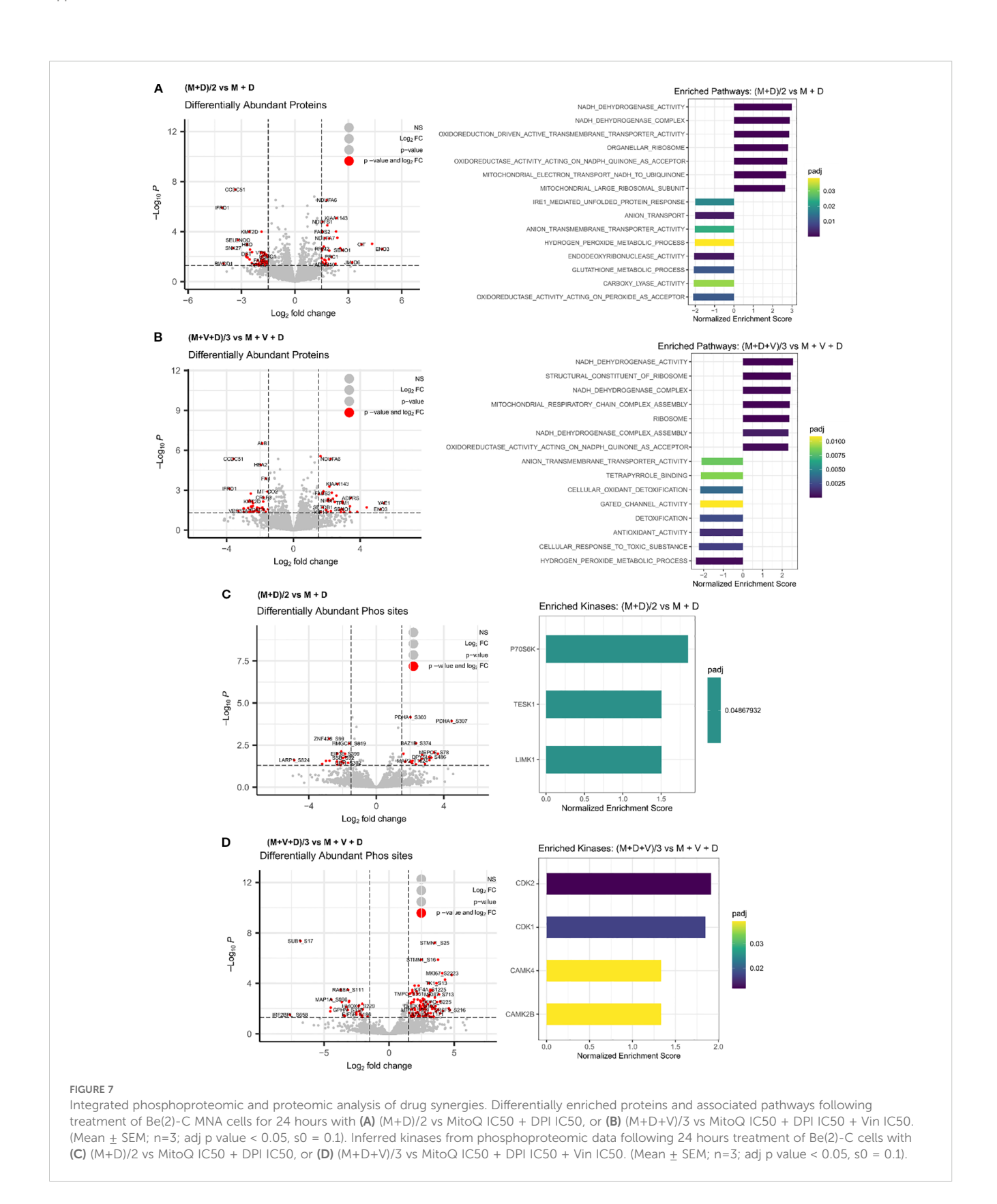
Overall, these results suggest that the effects of MitoQ, DPI, and vincristine are mediated mainly through OXPHOS inhibition, MYCN regulation, and disruptions in DNA damage response and cell cycle progression.

To identify the proteins and pathways modulated by the combination treatments versus the single treatments, we applied a linear regression model to the matched global proteomic and phosphoproteomic data (Figure 7). The model identifies pathways responsible for the effect of the double and triple drug combinations, versus the effect of the addition of each single agent at its IC50 concentration. The differentially expressed

proteins revealed that mainly the respirasome, mitochondrial ribosome, hydrogen peroxide and glutathione metabolic processes are responsible for the effect exerted by the double combination on Be(2)C cells (Figure 7A). Regarding the triple combination, the pathways are highly similar to those of (M+D)/2, with an additional enrichment in pathways associated with anion transmembrane transporter activity (Figure 7B). In terms of kinase enrichment, pathways related to cell cycle, DNA damage response, cell proliferation and regulation of cytoskeleton organization account for the effects of (M+D)/2 and (M+D+V)/3 compared to the addition of single agents (LIMK1, TESK1, P70S6K, CDK1, CDK2, CAMK4, CAMK2B) (Figures 7C, D). These findings suggest that the mechanism of synergy underlying the interaction between DPI and MitoQ is linked to their impact on mitochondrial metabolism and cell cycle regulation. Furthermore, the addition of vincristine does not significantly alter the proteomic profile linked to the activity of the other two compounds, while still causing more cell death when combined with MitoQ and DPI at a low dosage. The independent function of vincristine underscores the therapeutic potential for MitoQ and DPI to engage previously untargeted pathways involved in cancer progression.

### 2.7 Potential molecular mechanisms of drug synergies

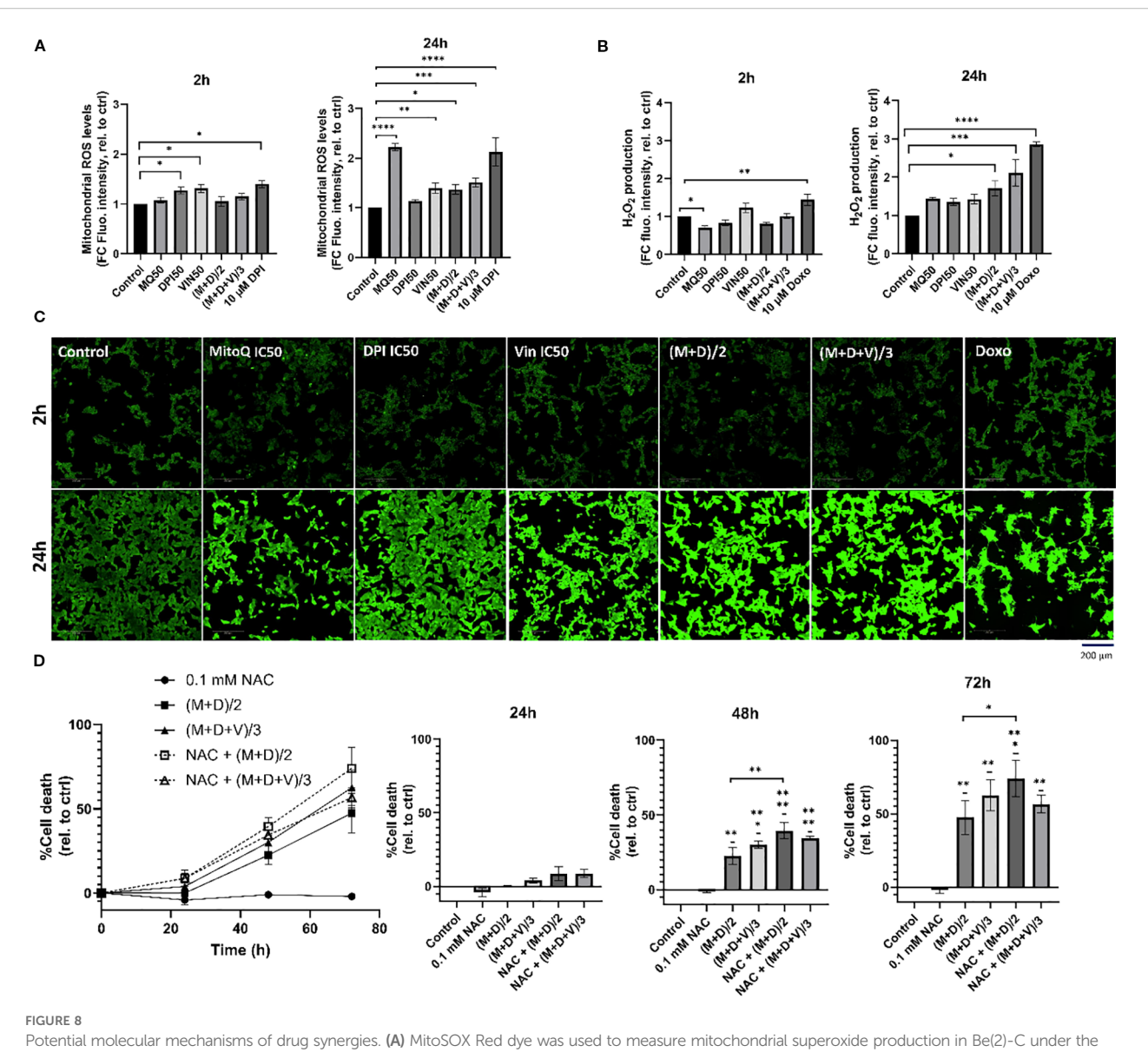
In both the double and triple drug combinations, processes generating ROS (NADH dehydrogenase, NADH quinone oxidoreductase/complex I) and antioxidant activities are significantly dysregulated (Figures 7A, B). Therefore, we examined superoxide and H<sub>2</sub>O<sub>2</sub> generation in MNA cells (Figure 8). Specifically, we exposed Be(2)-C cells to conditions akin to those used for MS analysis, utilizing either DPI, MitoQ and vincristine individually or in combination. Indeed, superoxide production has previously been demonstrated to be linked to the susceptibility of MNA NB cells to DPI, resulting in cytochrome c release, caspase activation, cytochrome c release and cell death (16). MitoSOX red dye (Invitrogen) was used as a probe to monitor mitochondrial superoxide, and Abgreen indicator (Abcam) for H<sub>2</sub>O<sub>2</sub>. The Abgreen indicator is a cell-permeable fluorescent indicator which generates green fluorescence when reacting with H<sub>2</sub>O<sub>2</sub>. 10 μM DPI was used as a positive control for superoxide production, while 10 µM doxorubicin was used as a positive control for H<sub>2</sub>O<sub>2</sub> generation. DPI, MitoQ, and vincristine at their IC50 concentrations individually increased mitochondrial superoxides over a 24-hour period (Figure 8A). Interestingly, MitoQ decreased H<sub>2</sub>O<sub>2</sub> after 2 hours of treatment, but this effect was reversed after 24 hours (Figure 8B). Both (M+D)/2 and (M+D+V)/3 combinations increased superoxide production after 24 hours, as well as H<sub>2</sub>O<sub>2</sub> (Figures 8A, B). Thus, the increase in H<sub>2</sub>O<sub>2</sub> production for the combinations after 24 hours reflects the enrichment analysis of the proteomics data, which indicate enhanced ROS production and less



ROS removal (Figure 7B). This also aligns with Figure 1B, where MitoQ partially reduced DPI-induced mitochondrial ROS but did not return levels to baseline; these residual ROS levels are sufficient to perturb metabolism and contribute to cell death alongside other mechanisms. These results further suggest that a balanced

generation of ROS by mitochondrial complex I is crucial to maintain MNA cellular fitness.

To determine whether  $\rm H_2O_2$  contributes to cell death, cells were pre-treated with 0.1mM N-acetylcysteine (NAC), a thiol-containing antioxidant that supports intracellular redox buffering, and



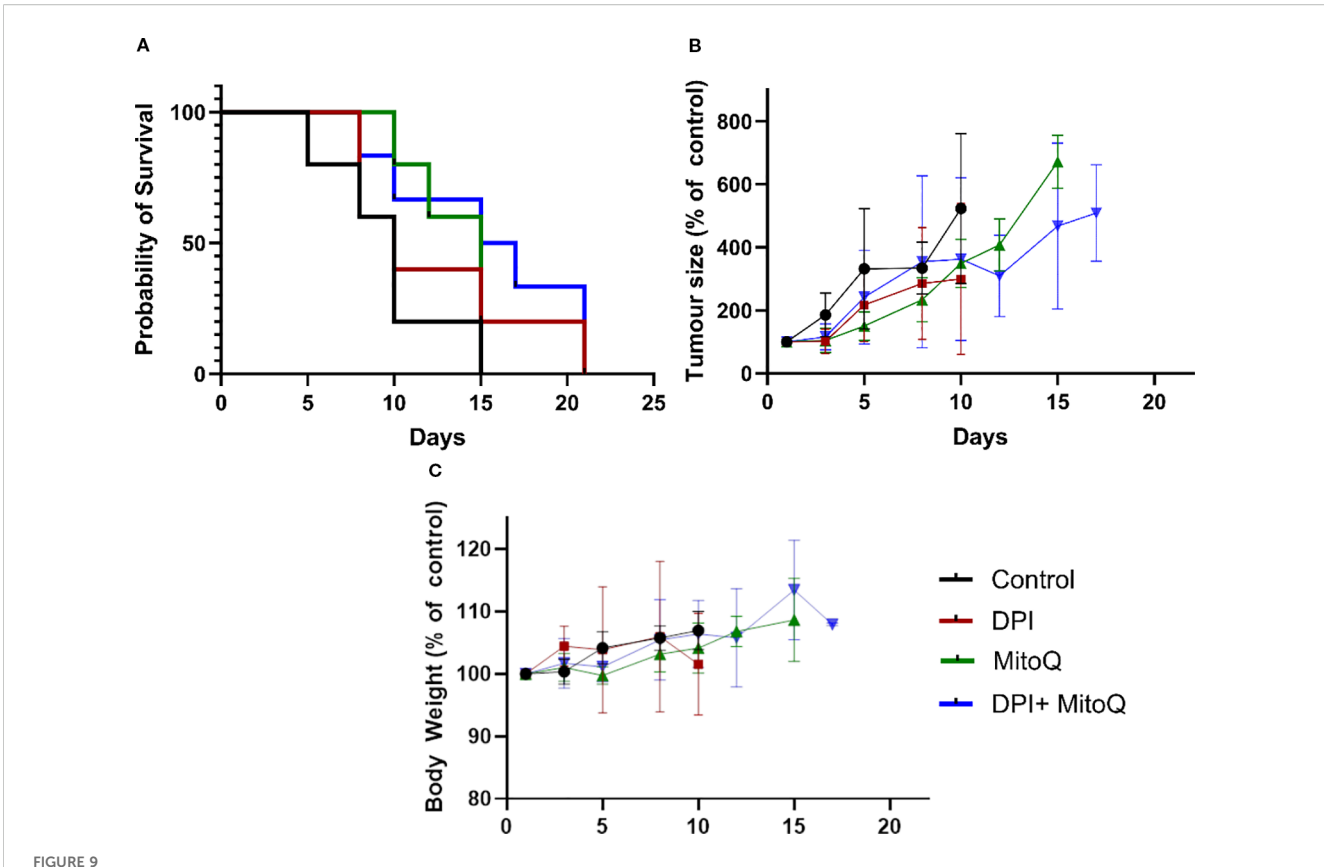
Potential molecular mechanisms of drug synergies. (A) MitoSOX Red dye was used to measure mitochondrial superoxide production in Be(2)-C under the same treatment conditions as in the proteomic analysis, for 2h, and 24h. 10  $\mu$ M DPI was used as a positive control for increase in mitochondrial superoxides (B, C) AbGreen indicator dye was used to measure  $H_2O_2$  production in Be(2)-C under the same treatment conditions as in the proteomic analysis. Doxorubicin was used as a positive control for  $H_2O_2$  induction. Below, associated confocal images x40. Scale bar = 200  $\mu$ M. (D) Cell death in Be(2)-C cells treated with NAC (0.1 mM) alone 1h prior to (M+D)/2 or (M+D+V)/3 addition measured with the CellTox Green indicator. (Mean  $\pm$  SEM; n=3; Ordinary One-Way ANOVA, p<0.05 = \*\*, p<0.005 = \*\*\*, p<0.0005 = \*\*\*\*, p<0.0001 = \*\*\*\*\*).

monitored over a 72-hour period (Figure 8D). NAC has been previously shown to rescue DPI-induced cell death (16), however, in the present experiments it failed to protect against the (M+D)/2 and (M+D+V)/3 combinations and instead further enhanced toxicity. While these results seem at odds with the common use of NAC as ROS scavenger, more recent literature shows that NAC also can enhance ROS generation under conditions, where cells express a certain pattern of enzymes that regulate ROS production (53), are co-treated with certain ROS generators (54), or suffer from mitochondrial stress (55). The latter situation is likely to occur in neuroblastoma cells co-treated with DPI and MitoQ and may explain the NAC mediated toxicity. The inability of NAC to rescue cell death in the combination treatments, despite its protective role in DPI-induced toxicity, underscores the complex

interplay between antioxidants and ROS-generating agents in cancer cells.

## 2.8 *In vivo* evaluation of MitoQ and DPI: tolerability and limited efficacy in NB mouse models

Finally, to evaluate the efficacy of MitoQ and DPI *in vivo*, both drugs were administered individually and in combination to Th-*MYCN* transgenic NB mice. Despite the promising efficacy observed in Th-*MYCN*-derived 3D spheres, administration of the compounds resulted in gastrointestinal toxicity, including blocked intestine and stomach enlargement, necessitating early termination



In vivo treatment of the IMR-5 xenograft immunodeficient NB mouse model. (A) Tumor size normalized to untreated control, measured over a 20-day treatment course with 3 mg/kg DPI, 30 mg/kg MitoQ, or their combination (1.5 mg/kg DPI and 20 mg/kg MitoQ). Efficacy curves terminate when 50% of the animals in a treatment arm had died. (B) Probability of survival for each treatment group, calculated based on survival events. (C) Body weight of animals for duration of the trial. Each treatment group consisted of at least 5 mice. Drugs were administered via oral gavage every two days. The endpoint of the trial was reached when the tumors grew to the size limit (15 mm in diameter). (Mean  $\pm$  SEM). Log-rank (Mantel-Cox) test p=0.2; Logrank test for trend p=0.0482; Gehan-Breslow-Wilcoxon test p=0.2087.

of the experiment. To address this limitation, the study was reconducted using an IMR-5 (MNA) xenograft immunodeficient NB mouse model, where a reduced toxicity was observed (Figures 9A, C). In contrast to our in vitro results, treatment with MitoQ, DPI, or their combination did not produce notable effects on tumor size reduction, even at the highest tolerable doses (Figure 9A). While a trend toward increased survival probability was observed in animals treated with either compound or their combination, the effect was not statistically significant (Figure 9B). These findings suggest that MitoQ and DPI are more tolerated in an in vivo immunodeficient environment, but their limited efficacy in reducing tumor burden may arise from challenges linked to oral administration, including poor absorption and first-pass metabolism. Alternatively, these findings may point to a role of the immune system in the effect of these drugs in vivo. We are currently investigating possible reasons for this discrepancy.

#### 3 Discussion

Targeting MYCN directly in NB has been challenging, primarily due to the absence of drug-binding pockets in MYCN. Using

combination therapies to target critical downstream signaling pathways is considered a rational approach.

In this paper, we initially focused on uncovering the mechanism of action of DPI, a NADPH oxidase inhibitor that we previously found to specifically inhibit MNA NB cell proliferation (16). DPI was found to increase mitochondrial superoxide production in MNA cells, leading to the induction of an apoptotic cascade (16). As a result, MitoQ was chosen as a mitochondria-specific ROS inhibitor to decrease superoxides and assess if it could reverse DPIinduced cell death on MNA cells. MitoQ is derived from the lipophilic molecule ubiquinone, allowing it to efficiently pass through lipid bilayers and accumulate within the inner mitochondrial membrane of cells (56, 57). Inside the mitochondrion, MitoQ undergoes redox cycling mediated by complex II, where it is reduced to mitoquinol, known for its potent antioxidant properties (58). Notably, this compound exhibits protective effects on normal cells (59) and is being investigated as a potential therapeutic agent for neurodegenerative and aging-related conditions (60, 61). Surprisingly, we found that MitoQ alone increased mitochondrial superoxide production. While it reduced high-dose DPI-mediated ROS, it did not prevent cell death of MNA NB cells. MitoQ exacerbated DPI-induced

cytotoxicity and was found toxic on its own at low nM concentrations. Consistent with these findings, other groups have shown that MitoQ can enhance superoxide production (62), and cause cytotoxicity in tumor cells (31, 63). Moreover, MitoQ appears to have a stronger inhibitory effect on cells with higher MYCN levels, similar to that observed with DPI (16). When administered alone, MitoQ increased neuronal differentiation of MNA NB cells, suggesting a transition towards a more "favorable" phenotype. Additionally, we observed strong synergism between DPI and MitoQ in reducing cell viability of MNA cells and a 3D MYCN-driven NB tumor model. The efficacy of the combination in a spheroid model of NB provides confidence that it may translate to in vivo models. These findings strongly suggest that MitoQ enhances the efficacy of DPI while also exhibiting antitumor activity as a standalone treatment in NB.

Kong et al., similarly uncovered synergy between a complex I inhibitor and a mito-antioxidant in cancer cells, suggesting their ability to reduce mitochondria-derived H2O2 levels as a potential mechanism of action (28). In our study, H2O2 levels increased after 24 hours of (M+D)/2 and (M+D+V)/3 treatments. We, therefore, believe that the observed cytotoxic effect may not be directly mediated by a reduction in  $H_2O_2$  in this context, but rather the opposite. MitoQ and DPI-induced damage to the respiratory chain may increase the NADH/NAD+ ratio over time, leading to O2 leakage and subsequent superoxide formation (64). Indeed, high reductive stress can paradoxically elevate superoxide levels via Glutathione Reductase (GSR) and Thioredoxin Reductase (TrxR) due to impaired electron flow caused by inhibitors (65). In line with these findings, we previously found that DPI (10 µM) increased Glutathione Peroxidase 1 (GPX1), GSR and Glutathione Synthetase (GSS) protein expression levels in MNA cells (16). Our linear regression model also highlighted antioxidant response and glutathione metabolic processes as key pathways responsible for the activity of MitoQ + DPI, which could be the result of a high  $H_2O_2$  production. Furthermore, it is crucial to note that superoxides are the primary but not the sole source of H<sub>2</sub>O<sub>2</sub>. H<sub>2</sub>O<sub>2</sub> is also generated via the peroxisome, endoplasmic reticulum, and certain NOX enzymes, such as NOX4 (66). Although it is difficult to conclude that ROS are the primary cause of apoptosis in this context, it is more likely that both DPI and MitoQ cause irreversible damage to OXPHOS in MNA cells (23, 31). Recent studies also demonstrated that redox-crippled MitoQ inhibited the proliferation and metastasis of breast cancer and glioma cells, suggesting that this effect is due to the inhibition of complex I rather than antioxidant properties (31, 67). "Redoxcrippled" MitoQ is a modified version of the mitochondrialtargeted antioxidant with its redox activity removed, allowing differentiation between effects from its antioxidant properties and other factors (31).

Adding vincristine to the MitoQ-DPI combination was motivated by its common use in the conventional clinical treatment of high-risk NB (68). Reducing the use and concentration of chemotherapeutic agents through combination therapy represents a key step towards less toxic treatments. We found that vincristine and DPI rather had an additive than a synergistic interaction. While synergism and additivity allow for

achieving better effects with lower drug concentrations, clinical data suggest that independent drug action can also significantly improve patient outcomes (69). One way of assessing drug synergy consists of combining drugs at half of their IC50 concentration for a two-drug combination, and one-third of their IC50 concentration for a three-drug combination (39, 70). Both (M+D)/2 and (M+D+V)/3 synergistically reduced cell viability in two MNA cell lines. These combinations also increased cell death and induced caspases 3/7 activation in all tested high-risk NB cells.

The use of MYCN-regulatable cell systems only moderately affected treatment sensitivity. In IMR-5/75 cells, MYCN downregulation still maintains amplification-level expression, which may explain the modest effect on treatment sensitivity. Interestingly, similar to DPI, MitoQ alone potently reduced MYCN levels in our most resistant NB cell line, Be(2)-C. Although the double and triple combinations at reduced doses did not decrease MYCN levels after 24 hours, they potently diminished MYCN protein levels in the IMR-5/75 cell line. Moreover, MitoQ was found to decrease MYCN phosphorylation at the Ser-156 residue. This phosphorylation site resides within a disordered region lacking a defined structure; thus, its functional implications remain unclear. The reduction of MYCN protein levels in MYCN-driven brain tumors is of major importance due to its central role as an oncogenic driver (71).

In addition to mitochondrial damage, whole proteomic and phosphoproteomic analysis highlighted the impact of our drug combinations on cell cycle blockade and DNA damage as part of their mechanism of action. Notably, vincristine showed minimal influence on the proteomic landscape altered by MitoQ + DPI combination. Interestingly, we consistently observed downregulation of RRM2 at the protein level across all single and combination treatments. Moreover, both (M+D)/2 and (M+D+V)/ 3 significantly decreased phosphorylation of RRM2 at Ser-80 and Ser-86 residues. RRM2 is an enzyme playing a crucial role in DNA synthesis and repair via deoxyribonucleotide production (49). Importantly, RRM2 is often found overexpressed in NB, and its depletion was shown to induce G1/S phase arrest due to replicative stress and checkpoint kinase 1 (CHK1) activation (47, 48). Elevated RRM2 levels also correlate with MYCN expression levels and poorer survival outcomes in NB patients (47). Although CHKs did not show differential expression at 24 hours post-treatment, it is plausible that such changes may manifest at later timepoints subsequent to RRM2 downregulation. (M+D)/2 and (M+D+V)/3 also upregulated the protein expression of mitochondrial Tetratricopeptide Repeat Domain 5 (TTC5/STRAP). TTC5 has previously been shown to downregulate ATP synthase activity, which sensitizes cells to mitochondrial-dependent apoptosis via enhanced p53 activity (72). This protein exerts a dual role, as it also accumulates in the nucleus following DNA damage, thereby enhancing the activity of p53 and leading to cell cycle and apoptosis. Moreover, TTC5 is a MYC interactor in acute myeloid leukemia stem cells, preventing excessive accumulation of MYC (73). While there is no direct evidence of TTC5 interaction with MYCN in NB, both proteins are direct interactors of the histone acetyltransferase p300 (74, 75).

Therefore, we propose that both combinations induce cytotoxicity through two potential mechanisms. The first one involves irreversible damage to the ETC, possibly through TTC5 upregulation, resulting in ATP loss, increased mitochondrial superoxide production and caspases 3/7 activation, and subsequent apoptosis. The second mechanism involves inhibition of clonogenic cell growth, potentially via downregulation of RRM2 and DNA damage, leading to accumulation of DNA breaks and cell cycle blockade. Microscopy experiments on a 3D spheroid model of MYCN-driven NB support this hypothesis. Indeed, an increase in DNA fragmentation and condensation was visible one day after the addition of M+D and M+D+V.

Several complex I inhibitors have been evaluated clinically and discontinued due to neurotoxicity and adverse side effects (IACS-010759, Tamoxifen, Piericidin A, Phenformin) (76, 77). MitoQ was found to induce mitochondrial damage in mouse kidney cortex tissue (78), although the concentrations used were much higher than the typical dosage used for cancer cells. However, over 400 peer-reviewed studies have reported on the therapeutic benefits of MitoQ, demonstrating its protective effects against a range of pathologies (79). Furthermore, MitoQ has been evaluated in several clinical trials and has shown overall good tolerability, with nausea and vomiting being the most commonly reported side effects (79). Additionally, MitoQ exhibits cardioprotective effects in rodents during doxorubicin-induced cardiac damage (80), or induced-sepsis (81). The major challenge seems to be establishing a standardized dosage of MitoQ for specific human diseases. Our results suggest that MitoQ can be used at low nanomolar concentrations across various MNA NB cell lines. In regard to DPI, we previously demonstrated that low micromolar concentrations effectively reduced tumor growth and metastasis in a MYCN-driven zebrafish model of NB, with low associated toxicity (16).

A limitation of this study is the discrepancy between the strong in vitro synergy of the MitoQ + DPI combination and its limited effectiveness in in vivo models of NB. The in vivo environment is considerably more complex, involving intricate biological networks and an active immune system, which are not present in in vitro cultures. Furthermore, gastrointestinal toxicity observed in the transgenic mice suggests that bioavailability may be compromised with oral administration. This can hinder drug effectiveness, as some drugs degrade in the acidic stomach environment or due to gut enzymes (82). While intravenous or intraperitoneal routes may improve bioavailability, they are difficult to apply in small animal models. The observed differences appear to be dependent on the animal model, as previous studies have shown that MitoQ is well tolerated at concentrations up to 500 µM in drinking water over several weeks, without causing adverse effects on behavior or metabolism (57, 83).

In conclusion, our data provides therapeutic opportunities for targeting MNA NB growth. The present study reveals that two mitochondria targeted agents, MitoQ and DPI were highly synergistic in reducing cell viability of MNA NB cells and MYCN-driven NB spheroids. MitoQ exhibited great antitumor

activity as a monotherapy against MNA cells, showing a MYCN-dependent effect similar to DPI. Moreover, we showed that MitoQ greatly decreased MYCN protein levels in MNA cells. The combination of MitoQ and DPI with a widely used chemotherapeutic agent allowed to more closely resemble potential clinical treatments for NB patients. Moreover, reducing drug dosage still achieved significant cytotoxic effects. Our data suggest that the tested drug combinations induce cell death in MNA cells through two mechanisms: inhibition of OXPHOS and cell cycle arrest. A common concern in drug synergy is the focus on combinations of agents with limited to null monotherapy activity (84). We demonstrate here that our single agents are highly effective at low concentrations on their own and show substantial synergistic effects when combined.

#### 4 Materials and methods

#### 4.1 Cell culture and in vivo experiments

#### 4.1.1 Cell lines

Four human NB cell lines were used in this paper: Be(2)-C (MNA), IMR5-/75-shMYCN (29) (MNA, doxycycline-inducible shRNA targeting MYCN, resulting in MYCN downregulation), IMR-32 (MNA), and SH-SY5Y/6TR(EU)/pTrex-Dest-30/MYCN (non-MNA, doxycycline-inducible transgene, resulting in MYCN overexpression). IMR-5/75-shMYCN and SH-SY5Y/6TR(EU)/ pTrex-Dest-30/MYCN are named IMR-5/75 and SH-SY5Y/ MYCN, respectively, in this paper. The cell lines were generously provided by Dr. Johannes Schulte and Dr. Frank Westermann. Cell lines were grown under standard tissue culture conditions in an incubator (37°C and 5% CO<sub>2</sub>). All cell lines were cultured in RPMI 1640 media (Gibco) supplemented with 10% Fetal Bovine Serum (FBS) (Gibco), 1% L-Glutamine (Gibco) and 1% Penicillin/ Streptomycin (Gibco). For IMR-5/75, the culture media was supplemented with 5  $\mu$ g/mL Blasticidin (Bio-Sciences) and 50  $\mu$ g/ mL Zeocin (Thermo Scientific) for plasmid selection. For SH-SY5Y/ MYCN, the culture media was supplemented with 7.5 µg/mL Blasticidin (Bio-Sciences) and 200 µg/mL Geneticin (G418) (Thermo Scientific) for selection of the plasmid. 1 µg/mL doxycycline (Sigma-Aldrich) was added to the media for 24 h to induce the expression of an shRNA against MYCN in IMR-5/75 cells and overexpress MYCN in SH-SY5Y/MYCN cells.

#### 4.1.2 3D spheroid NB model

The primary murine NB neurospheres were generously provided by Dr. Evon Poon and Prof. Louis Chesler (ICR, England). These cells were extracted from tumors coming from Th-*MYCN* transgenic mice over-expressing *MYCN* gene under the control of the tyrosine hydroxylase promoter. Spheroids were grown under standard tissue culture conditions in an incubator (37 °C and 5% CO<sub>2</sub>). The cells were cultured in Ultra-Low-Attachment plates (ULA) (Thermo Scientific) in PrimNeuS media (85).

#### 4.1.3 Mice and in vivo experiments

All animal experiments were approved by The Institute of Cancer Research Animal Welfare and Ethical Review Body and performed in accordance with the UK Home Office Animals (Scientific Procedures) Act 1986, the UK National Cancer Research Institute guidelines for the welfare of animals in cancer research and the ARRIVE (animal research: reporting *in-vivo* experiments) guidelines. Female NSG mice were obtained from Charles River and enrolled into trial at 6–8 weeks of age. Mice were maintained on a regular diet in a pathogen-free facility on a 12 h light/dark cycle with unlimited access to food and water.

One million IMR5 cells with 50% matrigel were injected subcutaneously into the right flank of NSG mice (female; 6–8 weeks old) and allowed to establish a murine xenograft model. Studies were terminated when the mean diameter of the tumor reached 15mm. Mice bearing IMR5 xenografts with a mean diameter of 5 mm were treated with 3 mg/kg DPI (P.O., 5 days/week), 30 mg/kg MitoQ (P.O., 3 days/week), or their combination (1.5 mg/kg DPI (P.O., 5 days/week) and 20 mg/kg MitoQ (P.O., 3 days/week)). Tumor volumes were measured by Vernier caliper across 2 perpendicular diameters, and volumes were calculated according to the following formula:  $V = 4/3\pi$  [(d1 + d2)/4]3 where d1 and d2 are the 2 perpendicular diameters. The endpoint of the trial was reached when the tumors grew to the size limit (15 mm in diameter).

#### 4.2 Chemicals

Mitoquinone Mesylate (MitoQ, MQ) was purchased from MedChemExpress (#HY-100116A), and Diphenyleneiodonium chloride (DPI) from Enzo Life Sciences (#BML-CN240-0010). Dimethyl sulfoxide (DMSO, vehicle) (#D2650), Vincristine Sulfate (Vin) (#V8388), N-acetyl-cysteine (#A15409) and retinoic acid (#R2625) were from Merck. Doxorubicin was purchased from Selleck Chemicals (#S1225).

#### 4.3 CellTox green assay

Cell toxicity was evaluated using the CellTox Green fluorescent assay (Promega). Typically, cells were seeded in 50  $\mu L$  media per well in duplicates on a black 96-well plate with clear bottom (Thermo Scientific). Complete RPMI phenol red-free media (Gibco) was used and was beforehand completed with CellTox Green Dye at a 1:500 ratio (v/v). Six h after seeding (or 24 h after doxycycline induction for MYCN-regulatable cell systems), the cells were treated with 50  $\mu L$  of drug(s) or vehicle and incubated at 37°C for 72 h. Fluorescence was measured at 4, 24, 48 and 72 h after treatment at 485 nm excitation and 530 nm emission on a SpectraMax M3 microplate reader (Molecular Devices).

#### 4.4 MitoSOX Red and PI stainings

Mitochondrial superoxide was measured with MitoSOX Red fluorescent indicator (Thermo Scientific). Propidum iodide (PI)

(Thermo Scientific) was used to selectively stain apoptotic cells. Typically, cells were seeded in 100 µL RPMI phenol red free media per well in duplicates on a black 96-well plate with clear bottom (Thermo Scientific). To prevent IMR-5/75 from detaching, the plates were treated beforehand with 100 µg/mL Poly-D-Lysine (Sigma-Aldrich). Six h after seeding (or 24 h after doxycycline induction for IMR-5/75), the cells were treated with 100 µL of drug(s) or vehicle and incubated at 37°C. After the appropriate incubation time, the cells were washed once with DPBS Ca<sup>2+</sup>/Mg<sup>2+</sup> (Invitrogen). MitoSOX Red dye (4 μM) or PI (1 μg/mL) were added together with Hoechst nuclear counterstain (1 μg/mL) (Bio-Sciences) to the cells in DPBS Ca<sup>2+</sup>/Mg<sup>2+</sup> and incubated for 20 minutes at 37 °C protected from light. The cells were washed twice with DPBS Ca2+/Mg2+, and fresh RPMI phenol redfree media was added before live cell imaging. MitoSOX Red indicator and PI were detected using the TRITC filter (Ex/Em: 396/610 nm) and Texas Red (Ex/Em:560/630), respectively, while Hoechst was detected using HOECHST 33342 filter (Ex/Em: 353/483).

#### 4.5 Live cell imaging

Confocal images of 4 optical planes interspaced by 1  $\mu$ m (from -1.0  $\mu$ m to 2.0  $\mu$ m included) across 25 x 25 fields of view with a 10% overlap were acquired per well on an Opera Phenix High Content Screening System (PerkinElmer) using a 40x or 63x/1.15 NA waterimmersion objective, with live cell parameters (37 °C and 5% CO<sub>2</sub>). The acquired images were analyzed using an optimized pipeline for each cell line on Harmony v.4.9 high-content analysis software (PerkinElmer). The building blocks within the software were used to identify and calculate the mean dye parameters per well: number of nuclei, MitoSOX Red, or PI mean intensity/cell.

#### 4.6 Neuronal differentiation

IMR-5/75 cells were plated in duplicates on a 6-well plate in 2 mL complete RPMI phenol red-free media (Gibco). One day after seeding, the cells were treated with either 50 nM MitoQ, 100 nM MitoQ, 10  $\mu$ M retinoic acid or vehicle, and incubated 37°C for 7 days. Every two days, the cells were treated with the appropriate drug or vehicle, in 2 mL fresh media. After 7 days, the cells were fixed, permeabilized and neuronal differentiation was assessed by Alexa Fluor 488 Phalloidin staining (Bio-Sciences) according to the manufacturer's instructions. Hoechst nuclear counterstain (1  $\mu$ g/mL) (Bio-Sciences) was used for nuclei counting. Imaging was performed on an EVOS Digital Inverted Fluorescence Microscope (Invitrogen), using the FITC (green) and the DAPI (blue) filters. Neurite outgrowth (cells with neurites >= 2 cell body diameters) were counted per cell using the NeuriteJ plugin of ImageJ (v1.53e; Java 1.8.0\_172).

#### 4.7 CellTiter-Glo assay

Cell viability by loss in ATP content was measured using the CellTiter-Glo Luminescent and CellTiter-Glo 3D Luminescent Cell Viability Assays (Promega). Cells were seeded in duplicates in 100  $\mu$ L

media on a Nunc 96-Well White Microplate (Fisher Scientific). Six h after seeding, the cells were treated with 100  $\mu L$  of drug(s) or vehicle and incubated at 37°C for 72 h. To assess cell viability of the neurospheres, cells were seeded after dissociation in 100  $\mu L$  PrimNeuS media on a Nunclon Sphera 96-Well U-Shaped-Bottom Microplate (Thermo Scientific). Two days after seeding, the cells were treated with 100  $\mu L$  of drug(s) or vehicle and incubated at 37°C for 72 h. CellTiter-Glo reagent was added to the wells according to the manufacturer's instructions and luminescent signal was measured on a SpectraMax M3 microplate reader (Molecular Devices).

#### 4.8 Caspase-Glo 3/7 assay

Caspases 3 and 7 activation were measured using Caspase-Glo 3/7 (Promega). Cells were seeded in duplicates in  $100~\mu L$  media on a Nunc 96-Well White Microplate (Fisher Scientific). Six h after seeding, the cells were treated with  $100~\mu L$  of drug(s) or vehicle and incubated at  $37^{\circ}$ C for 24 h. Caspase-Glo reagent was added to the wells according to the manufacturer's instructions and luminescent signal was measured on a SpectraMax M3 microplate reader (Molecular Devices).

#### 4.9 Western blotting

Six hours after seeding (or 24 h after doxycycline induction for IMR-5/75), the cells were treated with either MitoQ IC50, DPI IC50, Vin IC50, (M+D)/2, (M+D+V)/3 or vehicle and incubated at 37°C for 24 h. Cells were harvested using 110 μL ice cold lysis buffer containing 20 mM Tris-HCl (pH 7.5), 150 mM NaCl, 1 mM MgCl<sub>2</sub>, 1% (v/v) Triton X-100 and 10% (v/v) of protease and phosphatase inhibitor cocktail (Roche). After sample denaturation and electrophoresis, membranes were blocked with 5% milk in TBS-T (120 mM Tris-HCl, pH 7.4, 150 mM NaCl, and 0.05% Tween 20) for 1 h at room temperature. Target proteins were detected using primary antibodies at 1:1000 dilution overnight at 4°C (MYCN #sc-53993, Santa-Cruz Technologies; Phospho-Histone H3 (Ser10) #3465, Cell Signaling Technology; Phospho-Histone H2AX (Ser139) #05-636, Sigma-Aldrich; Cyclin B1 #12231, Cell Signaling Technology; Cyclin D1 #2922, Cell Signaling Technology; GAPDH #2118, Cell Signaling Technology). Anti-mouse or anti-rabbit secondary antibodies (Cell Signaling Technology) HRP-conjugated at 1:5000 dilution were incubated with the membranes for 1 h at room temperature, and visualized using a chemiluminescence system. GAPDH was used as a loading control.

#### 4.10 Synergy analysis

Synergy scores were calculated using SynergyFinder 3.0 for 2-drug combinations. Normalized cell viability values were imported to SynergyFinder 3.0 in a matrix format, and %viability was chosen as a readout. LL4 was selected for curve-fitting algorithm, detection of outliers was activated, and the Zero Interaction Potency (ZIP) or Loewe model were used to capture the drug interaction relationships.

To investigate the potential synergy of two or more drugs in combination at reduced doses, the Bliss Independence model was used. According to Rukhlenko et al. (39), the Bliss synergy score was defined as follows for reduced drug combinations:

According to the Bliss criterion, when two independent drugs are combined, their effects simply add up, and the Bliss synergy score is zero. In that case, if the combination is merely additive, the effect would be the following:

$$\mathbf{E}_{\mathsf{expA+B}} = \sqrt{\mathbf{E}_{\mathsf{A}}} \times \sqrt{\mathbf{E}_{\mathsf{B}}}$$

In this equation, E is the %viability effect obtained from the CellTiter-Glo output.  $E_{A+B}$  is the observed effect of the combined drugs, and  $E_A * E_B$  the expected effect when the drug effects are independent (viability values of the two single drugs). The Bliss synergy score was therefore calculated as follows:

$$S_{bliss} = E_{expA+B} - E_{obsA+B} = \sqrt{E_A} \times \sqrt{E_B} - E_{A+B}$$

In this context, a positive Bliss score means that the observed effect of the combination is lower than what would be anticipated if the drug effects were independent, thereby indicating synergy. In contrast, a negative Bliss score would suggest antagonism.

# 4.11 Total proteomics and phosphoproteomics analysis by liquid chromatography combined with tandem mass spectrometry

Be(2)-C cells were cultured in triplicates in 10 cm dishes and treated the following day either with MitoQ IC50, DPI IC50, Vin IC50, (M+D)/2, (M+D+V)/3, or vehicle for 24 h and washed once with PBS. Cells were lysed in 100 µL ice cold 8 M Urea/50 mM Tris HCl lysis buffer (Fisher Scientific) with 1:100 of Halt Cocktail Inhibitor, EDTA-free (100X) (Thermo Scientific). Samples were sonicated on ice twice for 9 seconds, at a power of 15% with a Skl-150IIDN Ultrasonic Homogenizer (Medical Supply Co. Ltd.), and protein concentration was measured using the Pierce BCA protein assay (Thermo Scientific). The same amount of protein (400  $\mu g$ ) were used for all samples, and 8 M Urea lysis buffer was used as a diluent if required. 8 mM of reducing agent DTT (Sigma) was then added to the samples and incubated in a thermomixer at 30°C for 30 minutes, followed by the addition of 20 mM iodoacetamide (Sigma) for protein carboxylation with incubation at 30°C in the dark for 30 minutes. Samples were diluted with 50 mM Tris-HCl to bring urea concentration down to below 2 M to prevent trypsin inhibition. Trypsin/Lys-C Mix, Mass Spec Grade (Promega) was added to the samples which were digested overnight at 37°C, on a thermomixer. Protein digestion was terminated by adding 100% formic acid to 1% final volume. Peptides were extracted from each sample using HyperSep C18 tips (Thermo Scientific), and 50 µg and 350 µg were kept for total proteomics and phosphoproteomics analysis, respectively.

Phospho-peptide enrichment was performed using TiO<sub>2</sub> (Titansphere Phos-TiO Bulk 10 um, GL Science), ratio of beads

to sample 10:1, mixed for 30 minutes at room temperature in 80% acetonitrile, 6% trifluoroacetic acid, 5 mM monopotassium phosphate, 20 mg/mL 2.5-dihydroxybenzoic acid. The phosphopeptides were eluted by adding 80  $\mu$ L of elution buffer directly (50% acetonitrile, 500 uL H<sub>2</sub>O, 7% Nh4OH ammonium hydroxide). Eluents were evaporated on the CentriVap Concentrator (Labconco) at 45°C for an hour. Peptides and phosphopeptides were analyzed separately by mass spectrometry.

Samples were analyzed on a time Tof Pro Mass Spectrometer (Bruker) as described previously (86).

The raw data was searched against the *Homo sapiens* subset of the Uniprot Swissprot database (reviewed) using the Fragpipe proteomics pipeline 21.1 with specific parameters for TIMS data-dependent acquisition (TIMS DDA). The normalized protein intensity of each identified peptide was used for label-free quantitation using the LFQ-MBR workflow. Within MSFraggers, precursor mass tolerance was set to +/-20ppm, fragment mass tolerance was set to +/-20ppm, tryptic cleavage specificity was applied, as well as fixed methionine oxidation and fixed N-terminal acetylation. Phospho-proteomic analysis was carried out using the LFQ-phospho workflow which includes phosphorylation as a variable modification on serine, threonine, and tyrosine residues (87).

### 4.12 Proteomics and phosphoproteomics data analysis using Perseus

Analysis for treatment versus untreated control of peptides and phosphopeptides was performed using Perseus v2.0.9.0. Phosphoproteomics results were normalized to the total proteomics. The data file from the Fragpipe output was loaded as a generic matrix in the software, with the Max LFQ intensities as main columns. The rows were filtered to remove the reverse proteins, the proteins only identified by site and the contaminants. The values were log2 transformed into normally distributed data. Rows were filtered based on the number of valid values: a minimum of 4 valid values out of 6 replicates in at least one group. Then, missing values were imputed from normal distribution by calculating width and center of the distribution. Statistical analysis was done using a One-Sample t-Test (s0 (fold change) = 0.1, FDR = 0.05). Kinase Substrate Enrichment Analysis (KSEA) was performed using the fgsea R package. Kinase-substrate relationships were obtained from the PhosphoSitePlus database and provided as gene sets (PhosphoSitePlus). Further protein-protein interaction and pathway enrichment analysis were done by exporting the final matrix to STRING database.

### 4.13 Pathway enrichment analysis using STRING

Upregulated and downregulated protein lists from each treatment condition versus untreated control were exported to the STRING database (https://string-db.org) for functional enrichment analysis and PPI network, using the k-means clustering method.

## 4.14 Linear regression model for mechanism of synergy of drug combinations

The Fragpipe combined\_proteins.txt file was filtered to remove known contaminants and protein groups containing no protein. Protein LFQ intensity values were log base 2 transformed, with zero values being assigned NaN to circumvent undefined values. Filtering was applied to keep only those proteins with at least four valid values in at least one drug treatment condition. NaN values were then reassigned to zero before median centering. Site- and condition-specific imputation was performed using the scImpute function in PhosR (88) if the protein was quantified in more than 50% of samples from the same drug treatment. Sample-wise tail-based imputation was implemented with the tImpute function (88). Linear regression through limma was used to model the relationship between protein abundance and drug treatment. The design matrix was coded as model.matrix(~treatment), with control samples representing the reference. Differential effects were identified by contrasting the coefficients from the combination drug treatment to the addition of each drug treatment in isolation. Differential protein abundance by empirical Bayes was performed to identify proteins reaching statistical significance. A signature of combination drug treatment synergy was created by selecting statically significant (adj p value < 0.05) and upregulated (LogFC > 0) genes from the above comparison. Gene set enrichment analysis (GSEA) was performed using the fgsea R package on the ontology gene sets retrieved from gseamsigdb.org (https://www.gsea-msigdb.org/gsea/msigdb). An FDR threshold of 0.1 was implemented.

#### 4.15 3D neuro-spheres imaging

Cells were seeded per well in 100  $\mu$ L PrimNeuS media on a Nunclon Sphera 96-Well U-Shaped-Bottom Microplate (Thermo Scientific). Four days after seeding, the cells were treated with MitoQ IC50 + DPI IC50, MitoQ IC50 + DPI IC50 + Vin IC50, or vehicle for 24 h. The spheres were washed once with PBS, then fixed in acetone, washed twice with PBS, and permeabilized using Triton X-100. The spheres were washed twice and stained with 1:500 PI solution (Bio-Sciences) supplemented with 250  $\mu$ g/mL RNAse A (Qiagen) and Hoechst nuclear counterstain (2  $\mu$ g/mL) (Bio-Sciences) for 30 min protected from light, at room temperature. Spheres were then washed once in PBS and imaged in fresh PBS on an Olympus IX83 Inverted Microscope (Mason Technology) using the TRITC (Ex/Em: 396/580 nm) and DAPI (Ex/Em: 353/483) filter sets. Image processing was performed on ImageJ (v1.53e; Java 1.8.0\_172).

#### 4.16 Statistics

All normalized values were transferred to GraphPad Prism 8.4.3 for statistical analysis of biological replicates. All graphs are represented as mean  $\pm$  SEM. Two-Way ANOVAs were used when using the IMR-5/75 and SH-SY5Y/MYCN -Dox/+Dox cell systems.

#### Data availability statement

The mass spectrometry proteomics and phosphoproteomics data generated in this study are in the process of being deposited to the ProteomeXchange Consortium via the PRIDE partner repository. The accession number will be provided and the dataset will be made publicly available upon publication.

#### **Ethics statement**

Ethical approval was not required for the studies on humans in accordance with the local legislation and institutional requirements because only commercially available established cell lines were used. The animal study was approved by The Institute of Cancer Research Animal Welfare and Ethical Review Body. The study was conducted in accordance with the local legislation and institutional requirements.

#### **Author contributions**

SE: Conceptualization, Formal Analysis, Investigation, Methodology, Validation, Visualization, Writing – original draft, Writing – review & editing. DE: Formal Analysis, Writing – review & editing. EP: Resources, Validation, Writing – review & editing. AA: Investigation, Writing – review & editing. KW: Methodology, Writing – review & editing. LC: Resources, Validation, Writing – review & editing. MH: Conceptualization, Funding acquisition, Project administration, Supervision, Writing – review & editing. WK: Conceptualization, Funding acquisition, Project administration, Supervision, Writing – review & editing.

#### **Funding**

The author(s) declare financial support was received for the research and/or publication of this article. This work received funding from Science Foundation Ireland and National Children's Research Centre/Children's Health Ireland through the Precision Oncology Ireland grant 18/SPP/3522, the Science Foundation Ireland Frontiers for the Future Program grant 22/FFP-A/10729, and with the financial support of Children's Health Foundation and under the management of Science Foundation Ireland under the Frontiers for the Future Program Grant Number 21/FFP-P/10130. Mass spectrometry was performed at The Comprehensive Molecular Analytical Platform which was funded by The SFI Research Infrastructure Program (18/RI/5702). Real-Time PCR

was performed at the Genomics Core facility of the UCD Conway Institute of Biomolecular and Biomedical Research. The Opera Phenix High Content Screening System (PerkinElmer) was used in the UCD Cell Screening laboratory, in UCD School of Biology and Environmental Science. LC and EP were funded by Cancer Research UK Discovery Programme Grant (A28278). LC was also funded by HEFCE/RAE. This project was partially supported by the Fight Kids Cancer Funding Programme, supported by Imagine for Margo, KickCancer, Fondatioun Kriibskrank Kanner, Federazione Italiana Associazioni Genitori e Guariti Oncoematologia Pediatrica (FIAGOP), and Cris Cancer Foundation.

#### Conflict of interest

The authors declare that the research was conducted in the absence of any commercial or financial relationships that could be construed as a potential conflict of interest.

#### Generative Al statement

The author(s) declare that no Generative AI was used in the creation of this manuscript.

Any alternative text (alt text) provided alongside figures in this article has been generated by Frontiers with the support of artificial intelligence and reasonable efforts have been made to ensure accuracy, including review by the authors wherever possible. If you identify any issues, please contact us.

#### Publisher's note

All claims expressed in this article are solely those of the authors and do not necessarily represent those of their affiliated organizations, or those of the publisher, the editors and the reviewers. Any product that may be evaluated in this article, or claim that may be made by its manufacturer, is not guaranteed or endorsed by the publisher.

#### Supplementary material

The Supplementary Material for this article can be found online at: https://www.frontiersin.org/articles/10.3389/fonc.2025.1613751/full#supplementary-material

#### References

- 1. Brodeur GM. Neuroblastoma: biological insights into a clinical enigma. *Nat Rev Cancer.* (2003) 3:203–16. doi: 10.1038/nrc1014
- 2. Park JR, Eggert A, Caron H. Neuroblastoma: biology, prognosis, and treatment. Hematology/Oncology Clinics North America. (2010) 24:65–86. doi: 10.1016/j.hoc.2009.11.011

- 3. Park JR, Bagatell R, London WB, Maris JM, Cohn SL, Mattay KM, et al. Children's Oncology Group's 2013 blueprint for research: Neuroblastoma. *Pediatr Blood Cancer*. (2013) 60:985–93. doi: 10.1002/pbc.24433
- 4. Friedman D, Henderson T. Late effects and survivorship issues in patients with neuroblastoma. *Children*. (2018) 5:107. doi: 10.3390/children5080107
- 5. Huang M, Weiss WA. Neuroblastoma and MYCN. Cold Spring Harbor Perspect Med. (2013) 3:a014415. doi: 10.1101/cshperspect.a014415
- 6. Ruiz-Pérez MV, Henley AB, Arsenian-Henriksson M. The MYCN protein in health and disease. *Genes (Basel)*. (2017) 8:113. doi: 10.3390/genes8040113
- 7. Epp S, Chuah SM, Halasz M. Epigenetic dysregulation in MYCN-amplified neuroblastoma. *Int J Mol Sci.* (2023) 24:17085. doi: 10.3390/iims242317085
- 8. Wang T, Liu L, Chen X, Shen Y, Lian G, Shah N, et al. MYCN drives glutaminolysis in neuroblastoma and confers sensitivity to an ROS augmenting agent. *Cell Death Dis.* (2018) 9:220. doi: 10.1038/s41419-018-0295-5
- 9. Oliynyk G, Ruiz-Pérez MV, Sainero-Alcolado L, Dzieran J, Zirath H, Gallart-Ayala H, et al. MYCN-enhanced oxidative and glycolytic metabolism reveals vulnerabilities for targeting neuroblastoma. *iScience*. (2019) 21:188–204. doi: 10.1016/j.isci.2019.10.020
- 10. Reczek CR, Chandel NS. The two faces of reactive oxygen species in cancer. *Annu Rev Cancer Biol.* (2017) 1:79–98. doi: 10.1146/annurev-cancerbio-041916-065808
- 11. Floros KV, Cai J, Jacob S, Kurupi R, Fairchild CK, Shende M, et al. MYCN-amplified neuroblastoma is addicted to iron and vulnerable to inhibition of the system Xc-/glutathione axis. *Cancer Res.* (2021) 81:1896–908. doi: 10.1158/0008-5472.CAN-20-1641
- 12. Alborzinia H, Flórez AF, Kreth S, Brückner LM, Yildiz U, Gartlgruber M, et al. MYCN mediates cysteine addiction and sensitizes neuroblastoma to ferroptosis. *Nat Cancer*. (2022) 3:471–85. doi: 10.1038/s43018-022-00355-4
- 13. Smith DJ, Cossins LR, Hatzinisiriou I, Haber M, Nagley P. Lack of correlation between MYCN expression and the Warburg effect in neuroblastoma cell lines. *BMC Cancer.* (2008) 8:259. doi: 10.1186/1471-2407-8-259
- 14. Brady SW, Liu Y, Ma X, Gout AM, Hagiwara K, Zhou X, et al. Panneuroblastoma analysis reveals age- and signature-associated driver alterations. *Nat Commun.* (2020) 11:5183. doi: 10.1038/s41467-020-18987-4
- 15. Dalton KM, Lochmann TL, Floros KV, Calbert ML, Kurupi R, Stein GT, et al. Catastrophic ATP loss underlies a metabolic combination therapy tailored for *MYCN* -amplified neuroblastoma. *Proc Natl Acad Sci USA*. (2021) 118:e2009620118. doi: 10.1073/pnas.2009620118
- 16. Epp S, Maher S, Aziz AAA, Marcone S, Egan D, Haapa-Paananen S, et al. Diphenyleneiodonium chloride inhibits MYCN-amplified neuroblastoma by targeting MYCN induced mitochondrial alterations. *bioRxiv*. (2003) 2024;2024.10.20.619268. doi: 10.1101/2024.10.20.619268v2
- 17. Li N, Ragheb K, Lawler G, Sturgis J, Rajwa B, Melendez JA, et al. DPI induces mitochondrial superoxide-mediated apoptosis. *Free Radical Biol Med.* (2003) 34:465–77. doi: 10.1016/S0891-5849(02)01325-4
- 18. Bloxham DP. The relationship of diphenyleneiodonium-induced hypoglycaemia to the specific covalent modification of NADH-ubiquinone oxidoreductase. *Biochem Soc Trans.* (1979) 7:103–6. doi: 10.1042/bst0070103
- 19. Pullar JM, Hampton MB. Diphenyleneiodonium triggers the efflux of glutathione from cultured cells\*. *J Biol Chem.* (2002) 277:19402-7. doi: 10.1074/jbc.M111053200
- 20. Lambert AJ, Buckingham JA, Boysen HM, Brand MD. Diphenyleneiodonium acutely inhibits reactive oxygen species production by mitochondrial complex I during reverse, but not forward electron transport. *Biochim Biophys Acta (BBA) Bioenergetics*. (2008) 1777:397–403. doi: 10.1016/j.bbabio.2008.03.005
- 21. Ojha R, Tantray I, Rimal S, Mitra S, Cheshier S, Lu B, et al. Regulation of reverse electron transfer at mitochondrial complex I by unconventional Notch action in cancer stem cells. *Dev Cell.* (2022) 57:260–276.e9. doi: 10.1016/j.devcel.2021.12.020
- 22. Li Y, Trush MA. Diphenyleneiodonium, an NAD(P)H oxidase inhibitor, also potently inhibits mitochondrial reactive oxygen species production. *Biochem Biophys Res Commun.* (1998) 253:295–9. doi: 10.1006/bbrc.1998.9729
- 23. Zavadskis S, Weidinger A, Hanetseder D, Banerjee A, Schneider C, Wolbank S, et al. Effect of diphenyleneiodonium chloride on intracellular reactive oxygen species metabolism with emphasis on NADPH oxidase and mitochondria in two therapeutically relevant human cell types. *Pharmaceutics*. (2020) 13:10. doi: 10.3390/pharmaceutics13010010
- 24. Jia J, Zhu F, Ma X, Cao ZW, Li YX, Chen YZ. Mechanisms of drug combinations: interaction and network perspectives. *Nat Rev Drug Discov.* (2009) 8:111–28. doi: 10.1038/nrd2683
- 25. Sun X, Vilar S, Tatonetti NP. High-throughput methods for combinatorial drug discovery. *Sci Trans Med.* (2013) 5:205rv1. doi: 10.1126/scitranslmed.3006667
- 26. Crystal AS, et al. Patient-derived models of acquired resistance can identify effective drug combinations for cancer. *Science*. (2014) 346:1480–6. doi: 10.1126/science.1254721
- 27. Franklin JL, McManus MJ, Murphy MP. Mitochondria-derived reactive oxygen species mediate caspase- dependent and-independent neuronal death. *Mol Cell Neurosci.* (2014) 63:13–23.

- 28. Kong H, Reczek CR, McElroy GS, Steinert EM, Wang T, Sabatini DM, et al. Metabolic determinants of cellular fitness dependent on mitochondrial reactive oxygen species. *Sci Adv.* (2020) 6:eabb7272. doi: 10.1126/sciadv.abb7272
- 29. Muth D, Ghazaryan S, Eckerle I, Beckett E, Pöhler C, Batzler J, et al. Transcriptional repression of SKP2 is impaired in MYCN-amplified neuroblastoma. *Cancer Res.* (2010) 70:3791–802. doi: 10.1158/0008-5472.CAN-09-1245
- 30. Liao PC, Franco-Iborra S, Yang Y, Pon LA. Live cell imaging of mitochondrial redox state in mammalian cells and yeast. *Methods Cell Biol.* (2020) 155:295–319.
- 31. Cheng G, Karoui H, Hardy M, Kalyanaraman B. Redox-crippled MitoQ potently inhibits breast cancer and glioma cell proliferation: A negative control for verifying the antioxidant mechanism of MitoQ in cancer and other oxidative pathologies. *Free Radical Biol Med.* (2023) 205:175–87. doi: 10.1016/j.freeradbiomed.2023.06.009
- 32. Le Gal K, Wiel C, Ibrahim MX, Henricsson M, Sayin VI, Bergo MO. Mitochondria-targeted antioxidants mitoQ and mitoTEMPO do not influence BRAF-driven Malignant melanoma and KRAS-driven lung cancer progression in mice. *Antioxidants.* (2021) 10(2):163.
- 33. Manohar CF, Salwen HR, Furtado MR, Cohn SL. Up-regulation of HOXC6, HOXD1, and HOXD8 homeobox gene expression in human neuroblastoma cells following chemical induction of differentiation. *Tumour Biol.* (1996) 17:34–47. doi: 10.1159/000217965
- 34. Voigt A, Zintl F. Effects of retinoic acid on proliferation, apoptosis, cytotoxicity, migration, and invasion of neuroblastoma cells. *Med Pediatr Oncol.* (2003) 40:205–13. doi: 10.1002/mpo.10250
- 35. Ianevski A, Giri AK, Aittokallio T. SynergyFinder 3.0: an interactive analysis and consensus interpretation of multi-drug synergies across multiple samples. *Nucleic Acids Res.* (2022) 50:W739–43.
- 36. Tang J, Wennerberg K, Aittokallio T. What is synergy? The Saariselkä agreement revisited. Front Pharmacol. (2015) 6. doi: 10.3389/fphar.2015.00181
- 37. Meyer CT, Wooten DJ, Lopez CF, Quaranta V. Charting the fragmented landscape of drug synergy. *Trends Pharmacol Sci.* (2020) 41:266–80. doi: 10.1016/j.tips.2020.01.011
- 38. Yadav B, Wennerberg K, Aittokallio T, Tang J. Searching for drug synergy in complex dose–response landscapes using an interaction potency model. *Comput Struct Biotechnol J.* (2015) 13:504–13. doi: 10.1016/j.csbj.2015.09.001
- 39. Rukhlenko OS, Halasz M, Rauch N, Zhernovkov V, Prince T, Wynne K, et al. Control of cell state transitions. *Nature*. (2022) 609:975–85. doi: 10.1038/s41586-022-05194-v
- 40. Liu Q, Yin X, Languino LR, Altieri DC. Evaluation of drug combination effect using a Bliss independence dose-response surface model. *Stat Biopharm Res.* (2018) 10:112–22. doi: 10.1080/19466315.2018.1437071
- 41. Duffy DJ, Krstic A, Halasz M, Schwarzl T, Konietzny A, Iljin K, et al. Retinoic acid and TGF- $\beta$  signalling cooperate to overcome MYCN-induced retinoid resistance. Genome Med. (2017) 9:15. doi: 10.1186/s13073-017-0407-3
- 42. Duffy DJ, Krstic A, Halasz M, Schwarzl T, Fey D, Iljin K, et al. Integrative omics reveals MYCN as a global suppressor of cellular signalling and enables network-based therapeutic target discovery in neuroblastoma. *Oncotarget.* (2015) 6:43182–201. doi: 10.18632/oncotarget.6568
- 43. Weiss WA, Aldape K, Mohapatra G, Feuerstein BG, Bishop JM. Targeted expression of MYCN causes neuroblastoma in transgenic mice. *EMBO J.* (1997) 16:2985–95. doi: 10.1093/emboj/16.11.2985
- 44. Rodrigues T, Kundu B, Silva-Correia J, Kundu SC, Oliveira JM, Reis RL, et al. Emerging tumor spheroids technologies for 3D *in vitro* cancer modeling. *Pharmacol Ther.* (2018) 184:201–11. doi: 10.1016/j.pharmthera.2017.10.018
- 45. Yasui M, Tanaka H, Seino Y. The role of tissue-fixed macrophages in apoptosis in the developing kidney. Nephron.~(1997)~77:325-32.~doi:~10.1159/000190296
- 46. Crowley LC, Marfell BJ, Waterhouse NJ. Analyzing cell death by nuclear staining with hoechst 33342. Cold Spring Harb Protoc. (2016) 2016. doi: 10.1101/pdb.prot087205
- 47. Nunes C, Depestel L, Mus L, Keller KM, Delhaye L, Louwagie A, et al. RRM2 enhances MYCN-driven neuroblastoma formation and acts as a synergistic target with CHK1 inhibition. *Sci Adv.* (2022) 8:eabn1382. doi: 10.1126/sciadv.abn1382
- 48. Zhan Y, Jiang L, Jin X, Ying S, Wu Z, Wang L, et al. Inhibiting RRM2 to enhance the anticancer activity of chemotherapy. *Biomedicine Pharmacotherapy.* (2021) 133:110996. doi: 10.1016/j.biopha.2020.110996
- 49. Zuo Z, Zhou Z, Chang Y, Liu Y, Shen Y, Li Q, et al. Ribonucleotide reductase M2 (RRM2): Regulation, function and targeting strategy in human cancer. *Genes Dis.* (2022) 11:218–33. doi: 10.1016/j.gendis.2022.11.022
- 50. Prichard MN. Function of human cytomegalovirus UL97 kinase in viral infection and its inhibition by maribavir. *Rev Med Virol.* (2009) 19:215–29. doi: 10.1002/rmv.615
- 51. Park CH, Kim KT. Apoptotic phosphorylation of histone H3 on Ser-10 by protein kinase C8. *PloS One*. (2012) 7:e44307. doi: 10.1371/journal.pone.0044307
- 52. Brustel J, Muramoto T, Fumimoto K, Ellins J, Pears CJ, Lakin ND. Linking DNA repair and cell cycle progression through serine ADP-ribosylation of histones. *Nat Commun.* (2022) 13:185. doi: 10.1038/s41467-021-27867-4

- 53. Mlejnek P, Dolezel P, Kriegova E, Pastvova N. N-acetylcysteine can induce massive oxidative stress, resulting in cell death with apoptotic features in human leukemia cells. *Int J Mol Sci.* (2021) 22:12635. doi: 10.3390/ijms222312635
- 54. Liao CY, Wu TC, Yang SF, Chang JT. Effects of NAC and gallic acid on the proliferation inhibition and induced death of lung cancer cells with different antioxidant capacities. *Molecules*. (2021) 27:75. doi: 10.3390/molecules27010075
- 55. Peris E, Micallef P, Paul A, Palsdottir V, Enejder A, Bauzá-Thorbrügge M, et al. Antioxidant treatment induces reductive stress associated with mitochondrial dysfunction in adipocytes. *J Biol Chem.* (2019) 294:2340–52. doi: 10.1074/ibc.RA118.004253
- 56. Kelso GF, Porteous CM, Coulter CV, Hughes G, Porteous WK, Ledgerwood EC, et al. Selective targeting of a redox-active ubiquinone to mitochondria within cells: antioxidant and antiapoptotic properties. *J Biol Chem.* (2001) 276:4588–96. doi: 10.1074/jbc.M009093200
- 57. Smith RAJ, Murphy MP. Animal and human studies with the mitochondria-targeted antioxidant MitoQ. *Ann New York Acad Sci.* (2010) 1201:96–103. doi: 10.1111/j.1749-6632.2010.05627.x
- 58. Kelso GF, Porteous CM, Hughes G, Ledgerwood EC, Gane AM, Smith R, et al. Prevention of mitochondrial oxidative damage using targeted antioxidants. *Ann New York Acad Sci.* (2002) 959:263–74. doi: 10.1111/j.1749-6632.2002.tb02098.x
- 59. Dhanasekaran A, Kotamraju S, Kalivendi SV, Matsunaga T, Shang T, Keszler A, et al. Supplementation of endothelial cells with mitochondria-targeted antioxidants inhibit peroxide-induced mitochondrial iron uptake, oxidative damage, and apoptosis. *J Biol Chem.* (2004) 279:37575–87. doi: 10.1074/jbc.M404003200
- 60. Rossman MJ, Santos-Parker JR, Steward CAC, Bispham NZ, Cuevas LM, Rosenberg HL, et al. Chronic supplementation with a mitochondrial antioxidant (MitoQ) improves vascular function in healthy older adults. *Hypertension*. (2018) 71:1056–63. doi: 10.1161/HYPERTENSIONAHA.117.10787
- 61. Gane EJ, Weilert F, Orr DW, Keogh GF, Gibson M, Lockhart MM, et al. The mitochondria-targeted anti-oxidant mitoquinone decreases liver damage in a phase II study of hepatitis C patients. *Liver Int.* (2010) 30:1019–26. doi: 10.1111/j.1478-3231.2010.02250.x
- 62. Doughan AK, Dikalov SI. Mitochondrial redox cycling of mitoquinone leads to superoxide production and cellular apoptosis. *Antioxid Redox Signal*. (2007) 9:1825–36. doi: 10.1089/ars.2007.1693
- 63. Rao VA, Klein SR, Bonar SJ, Zielonka J, Mizuno N, Dickey JS, et al. The antioxidant transcription factor nrf2 negatively regulates autophagy and growth arrest induced by the anticancer redox agent mitoquinone\*. *J Biol Chem.* (2010) 285:34447–59. doi: 10.1074/jbc.M110.133579
- 64. Murphy MP. How mitochondria produce reactive oxygen species. *Biochem J.* (2009) 417:1. doi: 10.1042/BJ20081386
- 65. P K, G C, Jn W. Increased reactive oxygen species production during reductive stress: The roles of mitochondrial glutathione and thioredoxin reductases. *Biochimica et biophysica acta*. (2015) 1847(6–7). Available from: https://pubmed.ncbi.nlm.nih.gov/25701705/.
- 66. Konno T, Melo EP, Chambers JE, Avezov E. Intracellular sources of ROS/H2O2 in health and neurodegeneration: spotlight on endoplasmic reticulum. *Cells.* (2021) 10:233. doi: 10.3390/cells10020233
- 67. Yoon NG, Lee H, Kim SY, Hu S, Kim D, Yang S, et al. Mitoquinone inactivates mitochondrial chaperone TRAP1 by blocking the client binding site. *J Am Chem Soc.* (2021) 143:19684–96. doi: 10.1021/jacs.1c07099
- 68. Smith V, Foster J. High-risk neuroblastoma treatment review. *Children (Basel)*. (2018) 5:114. doi: 10.3390/children5090114
- 69. Palmer AC, Sorger PK. Combination Cancer Therapy Can Confer Benefit via Patient-to-Patient Variability without Drug Additivity or Synergy. *Cell.* (2017) 171:1678–1691.e13. doi: 10.1016/j.cell.2017.11.009

- 70. Cokol-Cakmak M, Cetiner S, Erdem N, Bakan F, Cokol M. Guided screen for synergistic three-drug combinations. *PloS One.* (2020) 15:e0235929. doi: 10.1371/journal.pone.0235929
- 71. Borgenvik A, Čančer M, Hutter S, Swartling FJ. Targeting MYCN in molecularly defined Malignant brain tumors. *Front Oncol.* (2021) 10:626751. doi: 10.3389/fonc.2020.626751
- 72. Maniam S, Coutts AS, Stratford MR, McGouran J, Kessler B, La Thangue NB. Cofactor Strap regulates oxidative phosphorylation and mitochondrial p53 activity through ATP synthase. *Cell Death Differ*. (2015) 22:156–63. doi: 10.1038/cdd.2014.135
- 73. TTC5 is required to prevent apoptosis of acute myeloid leukemia stem cells. *Cell Death Dis.* 4:e573–e573.
- 74. DeMonacos C, Krstic-DeMonacos M, La Thangue NB. A TPR motif cofactor contributes to p300 activity in the p53 response. *Mol Cell.* (2001) 8(1):71–84. doi: 10.1016/S1097-2765(01)00277-5
- 75. Cheng C, He T, Chen K, Cai Y, Gu Y, Pan L, et al. P300 interacted with N-myc and regulated its protein stability via altering its post-translational modifications in neuroblastoma. *Mol Cell Proteomics*. (2023) 22:100504. doi: 10.1016/j.mcpro.2023.100504
- 76. Zhang X, Dang CV. Time to hit pause on mitochondria-targeting cancer therapies. Nat Med. (2023) 29:29–30. doi: 10.1038/s41591-022-02129-y
- 77. Kawada M, Amemiya M, Yoshida J, Ohishi T. The therapeutic potential of mitochondrial toxins. *J Antibiot*. (2021) 74:696–705. doi: 10.1038/s41429-021-00436-z
- 78. Gottwald EM, Duss M, Bugarski M, Haenni D, Schuh CD, Landau EM, et al. The targeted anti-oxidant MitoQ causes mitochondrial swelling and depolarization in kidney tissue. *Physiol Rep.* (2018) 6:e13667. doi: 10.14814/phy2.13667
- 79. Sulaimon LA, Afolabi LO, Adisa RA, Ayankojo AG, Afolabi MO, Adewolu AM, et al. Pharmacological significance of MitoQ in ameliorating mitochondria-related diseases. *Adv Redox Res.* (2022) 5:100037. doi: 10.1016/j.arres.2022.100037
- 80. Chandran K, Aggarwal D, Migrino RQ, Joseph J, McAllister D, Konorev EA, et al. Doxorubicin inactivates myocardial cytochrome c oxidase in rats: cardioprotection by mito-Q. *Biophys J.* (2009) 96:1388–98. doi: 10.1016/j.bpj.2008.10.042
- 81. Supinski GS, Murphy MP, Callahan LA. MitoQ administration prevents endotoxin-induced cardiac dysfunction. *Am J Physiol Regul Integr Comp Physiol.* (2009) 297:R1095–102. doi: 10.1152/ajpregu.90902.2008
- 82. Stielow M, Witczyńska A, Kubryń N, Fijałkowski Ł, Nowaczyk J, Nowaczyk A. The bioavailability of drugs—The current state of knowledge. *Molecules*. (2023) 28:8038. doi: 10.3390/molecules28248038
- 83. Rodriguez-Cuenca S, Cochemé HM, Logan A, Abakumova I, Prime TA, Rose C, et al. Consequences of long-term oral administration of the mitochondria-targeted antioxidant MitoQ to wild-type mice. *Free Radic Biol Med.* (2010) 48:161–72. doi: 10.1016/j.freeradbiomed.2009.10.039
- 84. Mason-Osann E, Pomeroy AE, Palmer AC, Mettetal JT. Synergistic drug combinations promote the development of resistance in acute myeloid leukemia. *Blood Cancer Discov.* (2024) 5:95–105. doi: 10.1158/2643-3230.BCD-23-0067
- 85. Cao D, Kishida S, Huang P, Mu P, Tsubota S, Mizuno M, et al. A new tumorsphere culture condition restores potentials of self-renewal and metastasis of primary neuroblastoma in a mouse neuroblastoma model. *PloS One*. (2014) 9:e86813. doi: 10.1371/journal.pone.0086813
- 86. D'Arcy C, Bass O, Junk P, Sevrin T, Oliviero G, Wynne K, et al. Disease–gene networks of skin pigmentation disorders and reconstruction of protein–protein interaction networks. *Bioengineering*. (2022) 10:13.
- 87. Yu F, Haynes SE, Teo GC, Avtonomov DM, Polasky DA, Nesvizhskii AI. Fast quantitative analysis of timsTOF PASEF data with MSFragger and ionquant. *Mol Cell Proteomics.* (2020) 19:1575–85. doi: 10.1074/mcp.TIR120.002048
- 88. Kim HJ, Kim T, Hoffman NJ, Xiao D, James DE, Humphrey SJ, et al. PhosR enables processing and functional analysis of phosphoproteomic data. *Cell Rep.* (2021) 34:108771. doi: 10.1016/j.celrep.2021.108771